ABSTRACT

TOWARDS A DUNE PHOTON DETECTION SYSTEM

Logan Clutch Jackson Rice, MS
Department of Physics
Northern Illinois University, 2018
Vishnu Zutshi, Director

The Deep Underground Neutrino Experiment (DUNE) will be sensitive to neutrino interactions in it liquid argon detector volume. Its primary objective is to measure mixing parameters relevant to neutrino oscillations. Another aspect of the primary science program is to measure neutrinos produced in core-collapse supernovae should one occur in the Milky Way Galaxy while the far detector is operational. The first 10kt module of DUNE will be a single phase Liquid Argon Time Projection Chamber (LarTPC). The goal of measuring neutrinos from supernovae requires an advanced photon detection system. Its design is driven by lessons from protoDUNE where testing of photon sensor components has been ongoing since at least 2016. It is also driven by simulations of supernova neutrino interactions.

NORTHERN ILLINOIS UNIVERSITY
DEKALB, ILLINOIS

AUGUST 2018

TOWARDS A DUNE PHOTON DETECTION SYSTEM

BY
LOGAN CLUTCH JACKSON RICE

A THESIS SUBMITTED TO THE GRADUATE SCHOOL

IN PARTIAL FULFILLMENT OF THE REQUIREMENTS

FOR THE DEGREE

MASTER OF SCIENCE

DEPARTMENT OF PHYSICS

Thesis Director:
Vishnu Zutshi

Acknowledgements

I would like to thank my adviser Vishnu Zutshi for his support, guidance, and advice throughout my time at NIU, Kurt Francis who taught me much about hardware during the testing of the protoDUNE SiPMs, Dan Boyden who designed the cold testing setup and procedure for dipping components in liquid nitrogen. I would not have made any progress with LArSoft without Alex Himmel and several others at Fermilab who guided and aided me during the photon detector simulations.

DEDICATION

To my family and their endless love and support

Table of Contents

List of Figures

List of Abbreviations

CERN	**C**onseil **E**uropéen **R**echerche **N**ucléaire
DUNE	**D**eep **U**nderground **N**eutrino **E**xperiment
FEB	**F**ront **E**nd **B**oard
FNAL	**F**ermi **N**ational **A**ccelerator **L**ab
GUT	**G**rand **U**nified **T**heory
LArTPC	**L**iquid **Ar**gon **T**ime **P**rojection **C**hamber
LBNF	**L**ong **B**aseline **N**eutrino **F**acility
MARLEY	**M**odel **A**rgon **R**eaction **L**ow **E**nergy **Y**ields
NICADD	**N**orthern **I**llinois **C**enter for **A**ccelerator and **D**etector **D**evelopment
PDE	**P**hoton **D**etection **E**fficiency
PE	**p**hoto **e**lectrons
PMT	**P**hoto **M**ultiplier **T**ubes
SASI	**S**tanding **A**ccretion **S**hock **I**nteractions
SiPM	**Si**licon **P**hoto **M**ultipliers
SSP	**S**iPM **S**ignal **P**rocessor
SURF	**S**anford **U**nderground **R**easearch **F**acility
TPB	**T**etra**P**henyl **B**utadienne
TPC	**T**ime **P**rojection **C**hamber
VUV	**V**acuum **U**ltra**V**iolet

Chapter 1

PHYSICS MOTIVATION

This thesis briefly describes the physics motivation of DUNE (in Chapter 1), describes the designs of DUNE and ProtoDUNE (in Chapter 2) with emphasis on the photon detection systems (Chapter 3). Next it describes the tests of the silicon photomultipliers (SiPM) which were installed in ProtoDUNE's photon detection system in 2018 (Chapter 4). This thesis ends with a discussion of the impact different photon detection designs could have in reconstructing time information of supernova neutrino interactions (Chapter 5).

The DUNE experiment has strong and diverse physics motivation. The foremost goal of the experiment is to measure neutrino oscillations. Other primary physics goals are to search for rare processes like proton decay, as well as make measurements of the neutrinos emitted from a supernova should one occur close enough to earth while the experiment is operational (see figure **??**) In this chapter we will briefly introduce the experiment in section 1.1. Because of the important role of neutrino oscillations to the DUNE experiment, we will next briefly touch on the history and theory of neutrinos and their oscillations in sections 1.2, 1.3, 1.4, and 1.5. We will merely mention proton decays in section 1.6. Supernova interactions rely heavily on the photon detection system (PDS). Modeling them has been extremely useful in influencing the design of this system. The PDS will be discussed throughout the thesis. Due to the the unique relevance of supernova physics to the DUNE photon detection design we will briefly discuss their history in section 1.7. Next we will quickly point out some of the many types of analyses which would be possible if we are given the incredible gift of a supernova during the operation of DUNE in section 1.8.

1.1 Introduction to the DUNE Experiment

The primary motivation behind the DUNE and LBNF program is to make precise measurements of neutrino oscillations. From these measurements a rich suite of studies will be possible. Some examples are measuring CP violation, determining absolute mass ordering, and searching for additional 'sterile' neutrinos that contribute to oscillations. In order to conduct these studies it is necessary to construct a long baseline neutrino beam (100's of miles), and to construct effective neutrino detectors near the source and far from the source. The LBNF will produce a wide energy spectrum of neutrinos in a beam generated at Fermi National Accelerator Laboratory (FNAL) in Batavia, Illinois, and direct them towards the Sanford Underground Research Facility (SURF) in Lead, South Dakota [1]. An effective neutrino baseline is achieved between the "near detector" located at FNAL and the "far detector" at SURF.

Neutrinos have famously low cross-sections of interaction. This low cross-section is a blessing to researchers attempting to understand oscillations. Such a long beam line is only possible because it can be directed through the crust of the Earth which offers negligible attenuation to the beam strength. In fact, based on cross section studies of neutrinos with nuclei, at many energies neutrinos could readily penetrate hundreds of light years of lead! The small cross section is also a curse. It is extremely difficult to actually detect these particles. The detection of neutrinos on the scale necessary to conduct the oscillation study requires monumental efforts. Atmospheric and cosmic backgrounds must be reduced by placing the detector nearly a mile underground at SURF. Additionally, in order to increase the chance of detecting any of the neutrinos which come from the beam, the detector volume must be enormous. The ultimate design of the DUNE far detector requires 40kt of active detector volume.

However the low-background and high detector volume are attractive in that they open the door for many studies outside of neutrino oscillation physics. Such a large and shielded detector system will be capable of conducting searches for proton decays which effectively probe energy

scales far beyond what particle accelerators will be able to directly produce. Proton decay limits could additionally have wide implications on the nature of dark matter, the cosmological evolution of the universe, and are predicted by several grand unified theories (GUTs).[1]

Additionally, the far detector will be sensitive enough to detect real time evolution of a large fraction of the energy spectrum of neutrinos produced in core collapse supernovae anywhere in the Milky Way Galaxy and in neighboring dwarf galaxies. Supernova physics is an active area of research with implications for astrophysics, nuclear physics, and cosmology. The supernova physics potential of DUNE is especially interesting in the context of this paper. Because neutrinos produced in neutronization bursts of supernovas are relatively low in energy and could appear at any moment, an advanced photon detection system is required to study them. The requirements of supernova physics are guiding the research, development, and design of the DUNE Far Detector Photon Detection System. [2]

1.2 Introduction to the Standard Model

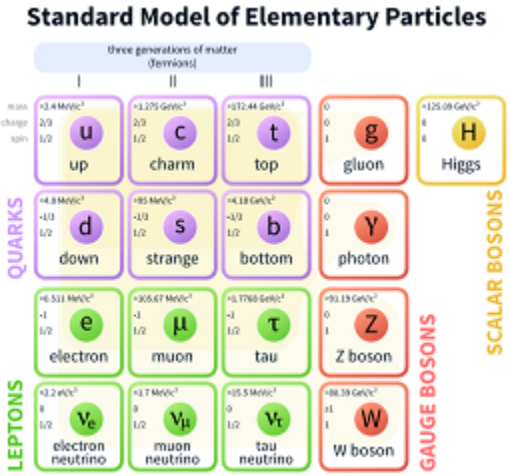

FIGURE 1.1: A brief summary of the standard model [[3]]

The Standard Model of Elementary Particles is a fundamental theory that enjoys strong experimental support. It describes all "normal matter" as interactions between six quarks and six leptons. The forces between all particles are mediated by the four gauge bosons. The masses of all the particles (except neutrinos) are known and can be described in terms of their coupling with the Higgs boson. The nature and amount of mass of the neutrinos remains a mystery. In addition to these 17 particles, each of the quarks, leptons, neutrinos, and the W boson have symmetric but opposite antiparticles. This brings the total to 30 fundamental particles. Accelerator facilities have subjected the standard model to rigorous tests throughout the last several decades. It has proven to be remarkably robust. However, no one believes that it is a complete theory. In fact the model has several flagrant shortcomings. It predicts nearly perfect symmetry between matter and antimatter, which seems to contradict what we know about the universe being made almost entirely of matter. It fails to predict what the masses of many of the fundamental particles ought to be. This is particularly embarrassing in the case of neutrinos where experimentalists have likewise failed to measure such a basic parameter. Furthermore it can not even account for all the matter in the universe. Based on numerous varieties of astronomical measurements, it is observed that there is about 5 times more dark matter than normal matter in the universe. Little of this dark matter is expected based on our current understanding of the Standard Model. This staggering amount of dark matter is dwarfed by observations that the expansion of the universe is speeding up, not slowing down, implying some dark energy source is driving it. Neutrino physics is an attractive possible bridge between what we now understand to new physics beyond the standard model.

Neutrinos are the only particles for which we have observed physics that is not predicted by the standard model (neutrino oscillations). They are fascinating because we know so little about them (not even their mass) despite the fact that they are the most common massive particle in the universe. In fact, many trillions of neutrinos pass through your body all of the time. Based on what we already know about neutrino oscillations, there is a mechanism for charge-parity violation. The violation of this symmetry is exactly what is needed to create a universe dominated by matter over antimatter. Furthermore, precise measurements of neutrino oscillations could reveal the existence of more neutrino states. If these states are massive enough, they could very well be

major contributors to dark matter which we observe in astrophysics. Furthermore, due to their feeble interactions, they can pass through matter that would attenuate any other type of particle. This has already been decisively useful for studies of stellar and supernova physics, as well as for the search for extreme processes that occur in Milky Way's galactic center. Neutrinos are not blocked by the outer layers of stars nor by the dust obscuring our view of the galactic center.

1.3 History of Neutrino Physics

In the 1910's - 1920's numerous experiments studied the newly discovered beta decay reaction. Several isotopes were known to undergo this reaction, and it was understood that a nucleus converts to another element with one more unit of charge while emitting an electron. If the masses of the mother and daughter isotopes were precisely known, the change in mass should be carried away by the energy of the outgoing electron. It was expected that this electron should have a discrete energy precisely corresponding to this mass difference. Measurements of the emitted electron showed that it did not possess a discrete energy but was emitted with a spectrum. Even more confounding, the high energy end point was always less than the energy associated with the mass difference of the mother and daughter isotopes.

In 1930 Pauli famously proposed an invisible, extremely light, neutral particle in a letter to a physics conference. This invisible particle would be a third object in the beta decays and would explain the energy anomaly. Having made this provocative suggestion, Pauli went on to just as famously explain he would skip the conference to attend a ball. In 1934 Fermi published a more complete theory of beta decay building on the particle that Pauli described calling it a neutrino.

In 1946 Pontecorvo suggested using a chlorine detector to search for neutrinos on his intuition that the reverse of the beta decay process should also occur and that the reverse beta decay would convert chlorine-37 to the unstable isotope argon-37 whose signature radioactive decay could be measured [4]. This design was tested at Brookhaven by Ray Davis in 1955. As we now know this was doomed to failure on the basis that the tiny light particle involved in a beta decay process is not in fact a neutrino but an antineutrino. At the time it was not obvious that the two should be distinct particles. Davis will find another application for this method later in his career. [5]

The first experiment that was able to measure antineutrino capture was performed by Reines and Cowan [6] who thankfully used the Savannah River nuclear reactor as their source of antineutrinos instead of a nuclear bomb test (as they had originally planned!) [4]

The existence of a second flavor of neutrino (the muon neutrino, ν_μ) was confirmed in 1962 at Brookhaven by Lederman, Schwartz, Steinberger. Though the existence of the tau neutrino (ν_τ) could not be confirmed until 2000 by the DONUT experiment at Fermilab. Before the existence of the separate neutrino flavors was even confirmed, Pontecorvo had already proposed a mechanism by which one type of neutrino could oscillate to another type. His ideas were greatly expanded upon by Maki, Nakagawa, and Sakata in 1962. These outlandish ideas about neutrino mixing gained traction as the Solar Neutrino Problem became more and more embarrassing. The Solar Neutrino Problem initially appeared due to the discrepancy between theoretical predictions of solar neutrino fluxes calculated from understanding the nuclear processes occuring in the sun and the fluxes observed by Ray Davis using an underground chlorine detector. His famous solar neutrino experiment was housed at the Homestake Mine in Lead, SD in 1968 [4]. In essence, Davis measured about a third of the neutrinos which were predicted.

As physicists argued whether the Davis experiment was definitive proof of neutrino mixing and experimentalists scratched their heads over what the next generation of detectors should attempt to probe, a surprise came in 1987. The Kamiokande II experiment (in Japan), the IMB experiment (in the United States), and Baksan (in Russia) simultaneously measured a burst of neutrinos in a period of only a few seconds. This burst was coincident with an observed type II supernova in the nearby (168,000 ly) Large Magellanic Cloud dwarf galaxy. The energy spectrum of these neutrinos matches the spectrum of neutrinos which should be produced during the neutronization process of stellar collapse. This was an exciting moment for neutrino physics.

The issue of neutrino mixing was decisively settled during the turn of the century. The Super-Kamiokande detector was built which was more efficient than the Homestake experiment. Additionally it was sensitive not only to electron neutrinos but to all three flavors (though with different efficiencies per flavor and it was not possible to measure the different fluxes independently). Its

results were published in 1998 [7]. Smoking gun evidence came from the Sudbury Neutrino Observatory in Canada in 2001. They published measurements made with a heavy water detector which could measure both total neutrino flux as well as electron neutrino flux independently. Neutrino oscillations were now a well-confirmed physical process.

The process is basically the same as what Pontecorvo originally suggested and is still paramaterized in a similar form to what Maki, Nakagawa, and Sakata developed in 1962. It is paramaterized with a single 3 x 3 matrix called the PMNS matrix or U_{PMNS} named for the initials of its originators. During the last two decades, the PMNS matrix was studied with great detail by groups like KAMland, Daya Bay, RENO, Minos and others. The way this matrix is studied will be the topic of discussion in the next section.

Neutrino physics is nearly 100 years old and remains a difficult and exciting field. The current generation of experiments make precise measurements of neutrino cross sections, oscillation parameters, and validate research and development efforts aimed at ever more ambitious detectors, like DUNE. The field is increasingly influencing and incfluenced by other subfields such as nuclear and astro-physics.

1.4 Neutrino Mixing and Neutrino Mass

With the resolution of the solar neutrino problem, Nobel Prizes were duly awarded to the leaders of the Homestake (Ray Davis in 2002), Super-Kamiokande (Takaaki Kajita in 2015), and SNO experiments (Art McDonald in 2015). Consequently neutrino oscillations became a well established scientific fact. It is worth discussing the theory of this phenomenon first proposed by Pontecorvo and later developed by Maki, Nakagawa, and Sakata. The basic idea is that the neutrino eigenstates that are relevant to the weak interaction vertex are different from the energy (or mass) eighenstates of propagating neutrinos. A neutrino interacting with a vector boson then has a definite flavor composition (ν_e, ν_μ, or ν_τ) but exists in a super position of mass eigenstates (ν_1, ν_2, or ν_3). Specifically a neutrino produced in association with an electron may be written as

$$|\nu_e\rangle = c_1 |\nu_1\rangle + c_2 |\nu_2\rangle + c_3 |\nu_3\rangle \tag{1.1}$$

More generally, any superposition flavor states can be expressed as a superposition of mass states and vice versa via the expression

$$|flavor\rangle = U_{PMNS}\,|mass\rangle \tag{1.2}$$

or

$$|mass\rangle = U^{\dagger}_{PMNS}\,|flavor\rangle\,. \tag{1.3}$$

Where U_{PMNS} is a 3 x 3 unitary matrix. We can write more explicit versions of the previous two expressions.

$$\begin{pmatrix} \nu_e \\ \nu_\mu \\ \nu_\tau \end{pmatrix} = \begin{pmatrix} U_{e,1} & U_{e,2} & U_{e,3} \\ U_{\mu,1} & U_{\mu,2} & U_{\mu,3} \\ U_{\tau,1} & U_{\tau,2} & U_{\tau,3} \end{pmatrix} \begin{pmatrix} \nu_1 \\ \nu_2 \\ \nu_3 \end{pmatrix} \tag{1.4}$$

and

$$\begin{pmatrix} \nu_1 \\ \nu_2 \\ \nu_3 \end{pmatrix} = \begin{pmatrix} U^*_{e,1} & U^*_{\mu,1} & U^*_{\tau,1} \\ U^*_{e,2} & U^*_{\mu,2} & U^*_{\tau,2} \\ U^*_{e,3} & U^*_{\mu,3} & U^*_{\tau,3} \end{pmatrix} \begin{pmatrix} \nu_e \\ \nu_\mu \\ \nu_\tau \end{pmatrix} \tag{1.5}$$

Since the PMNS matrix represents a rotation from one three dimensional space to another, it is tempting and convenient to write it as a classical rotation matrix R defined by three Euler angles, θ_{12}, θ_{13}, and θ_{23}.

$$R = \begin{pmatrix} 1 & 0 & 0 \\ 0 & cos(\theta_{23}) & sin(\theta_{23}) \\ 0 & -sin(\theta_{23}) & cos(\theta_{23}) \end{pmatrix} \times \begin{pmatrix} cos(\theta_{13}) & 0 & sin(\theta_{13}) \\ 0 & 1 & 0 \\ -sin(\theta_{13}) & 0 & cos(\theta_{13}) \end{pmatrix} \times \begin{pmatrix} cos(\theta_{12}) & sin(\theta_{12}) & 0 \\ -sin(\theta_{12}) & cos(\theta_{12}) & 0 \\ 0 & 0 & 1 \end{pmatrix} \tag{1.6}$$

Despite the attractiveness of this notation, it does not quite contain all of the information that we need. In particular, given that U_{PMNS} is a unitary matrix it should in general be complex. It turns out that we can factor out most complex phases into definitions for the spinors which

represent the neutrinos. However we are still left with at least one complex phase. The U_{PMNS} matrix is conventionally written as

$$\begin{pmatrix} 1 & 0 & 0 \\ 0 & cos(\theta_{23}) & sin(\theta_{23}) \\ 0 & -sin(\theta_{23}) & cos(\theta_{23}) \end{pmatrix} \times \begin{pmatrix} cos(\theta_{13}) & 0 & sin(\theta_{13})e^{-i\delta} \\ 0 & 1 & 0 \\ -sin(\theta_{13})e^{i\delta} & 0 & cos(\theta_{13}) \end{pmatrix} \times \begin{pmatrix} cos(\theta_{12}) & sin(\theta_{12}) & 0 \\ -sin(\theta_{12}) & cos(\theta_{12}) & 0 \\ 0 & 0 & 1 \end{pmatrix}. \tag{1.7}$$

Where we have included the complex phase term, δ, in the second matrix. Multiplying this through gives us the PMNS matrix written in terms of just three angles and one complex phase [8]. To save space we'll adopt the notation $cos(\theta_{13}) = c_{13}$, $sin(\theta_{23}) = s_{23}$, etc.

$$U_{PMNS} = \begin{pmatrix} U_{e,1} & U_{e,2} & U_{e,3} \\ U_{\mu,1} & U_{\mu,2} & U_{\mu,3} \\ U_{\tau,1} & U_{\tau,2} & U_{\tau,3} \end{pmatrix} = \begin{pmatrix} c_{12}c_{13} & c_{12}c_{13} & s_{13}e^{-i\delta} \\ -s_{12}c_{23} - c_{12}s_{23}s_{13}e^{i\delta} & s_{12}c_{23} - c_{12}s_{23}s_{13}e^{i\delta} & c_{23}c_{13} \\ s_{12}c_{23} - c_{12}s_{23}s_{13}e^{i\delta} & -s_{12}c_{23} - c_{12}s_{23}s_{13}e^{i\delta} & c_{23}c_{13} \end{pmatrix} \tag{1.8}$$

Imagine that a antineutrino is produced in association with an electron with energy E. Perhaps this antineutrino is about 4 MeV and was produced the beta decay process $Th \rightarrow Po + e^- + \bar{\nu}_e$ at a nuclear power station. At the instant it is emitted, it is a pure electron antineutrino. Using elements from the PMNS matrix we could write

$$|\psi(0)\rangle = |\bar{\nu}_e\rangle = \sum_k^3 U_{e,k} |\nu_k\rangle = U_{e,1} |\nu_1\rangle + U_{e,2} |\nu_2\rangle + U_{e,3} |\nu_3\rangle . \tag{1.9}$$

[1]

Now we want to describe how this state evolves in time. For simplicity lets use units where $\hbar = c = 1$. The best limits on neutrino masses indicate that they are $m_\nu \leq 2$ eV which means that even "low energy" neutrinos of a few MeV exist in the ultrarelativistic regime [4].

[1] By convention, antineutrinos couple to the weak interaction vertex as spinors and neutrinos couple as their adjoints. This will be important later. [8]

$$E = \sqrt{p^2 + m^2} = p\sqrt{1 + \frac{m^2}{p^2}} \tag{1.10}$$

The Taylor series expansion of $\sqrt{1+x} = 1 + \frac{x}{2} + ...$ Since we've already established $m << p$ we can take the first two terms with $x = \frac{m^2}{p^2}$ and continue exploiting the inherent ultrarelativistic situation to simplify our expression

$$E \approx p + \frac{m^2}{2p} \approx p + \frac{m^2}{2E}. \tag{1.11}$$

Now the general time evolution for a quantum state of some energy can be described in terms of a phase

$$\phi = E \cdot t - p \cdot x. \tag{1.12}$$

Consider a neutrino interaction that occurs a time T and distance L away from the neutrino's source. Because we are in an ultrarelativistic regime, $T \approx L$ is a safe approximation. Plugging equation 1.11 and $x = t = L$ into equation 1.12

$$\phi = p \cdot L + \frac{m^2 L}{2E} - p \cdot L = \frac{m^2 L}{2E} \tag{1.13}$$

And now we can write a "time" dependent (or distance dependent) version of equation 1.9.

$$|\psi(L)\rangle = \sum_k^3 U_{e,k} \, |\nu_k\rangle \, e^{im_k^2 L/2E} \tag{1.14}$$

Since the mass composition of the neutrino evolves, so must the flavor composition. In other words, this neutrino may no longer behave like an electron neutrino at distances away from its source. This can be seen explicitly by using equation 1.5 to express this evolution in terms of the flavor eigenstates.

$$|\psi(L)\rangle = \sum_k^3 U_{e,k} \Big(U_{e,k}^* \, |\bar{\nu}_e\rangle + U_{\mu,k}^* \, |\bar{\nu}_\mu\rangle + U_{\tau,k}^* \, |\bar{\nu}_\tau\rangle \Big) e^{im_k^2 L/2E} \tag{1.15}$$

To better see how the flavor eigenstates evolve lets group the terms of the previous expression into the three flavor states ($\alpha = e, \mu, \tau$) rather than mass states.

$$|\psi(L)\rangle = \sum_{\alpha}^{e,\mu,\tau} \left(U^*_{\alpha,1} U_{e,1} e^{im_1^2 L/2E} + U^*_{\alpha,2} U_{e,2} e^{im_2^2 L/2E} + U^*_{\alpha,2} U_{e,2} e^{im_2^2 L/2E} \right) |\bar{\nu}_\alpha\rangle \tag{1.16}$$

Now we can write an expression for the probability of our antineutrino oscillating to another flavor. For example

$$P(\bar{\nu}_e \to \bar{\nu}_\mu) = |\langle \bar{\nu}_\mu | \psi(L) \rangle|^2 = \left| (U^*_{\mu,1} U_{e,1} e^{im_1^2 L/2E} + U^*_{\mu,2} U_{e,2} e^{im_2^2 L/2E} + U^*_{\mu,2} U_{e,2} e^{im_2^2 L/2E}) \right|^2 \tag{1.17}$$

This expression may be simplified by recalling that the PNMS matrix is unitary and therefore

$$U_{e,1} U^*_{\mu,1} + U_{e,2} U^*_{\mu,2} + U_{e,3} U^*_{\mu,3} = 0. \tag{1.18}$$

Now apply the following complex number identity

$$|z_1 + z_2 + z_3|^2 = |z_1|^2 + |z_2|^2 + |z_3|^2 + 2Re[z_1 z_2^* + z_1 z_3^* + z_2 z_3^*] \tag{1.19}$$

to both equation 1.17

$$\begin{aligned} P(\bar{\nu}_e \to \bar{\nu}_\mu) = {} & |U^*_{\mu,1} U_{e,1}|^2 + |U^*_{\mu,2} U_{e,2}|^2 + |U^*_{\mu,3} U_{e,3}|^2 + 2Re[U^*_{\mu,1} U_{e,1} U_{\mu,2} U^*_{e,2} e^{-i(m_1^2 - m_2^2)L/2E}] \\ & + 2Re[U^*_{\mu,1} U_{e,1} U_{\mu,3} U^*_{e,3} e^{-i(m_1^2 - m_3^2)L/2E}] + 2Re[U^*_{\mu,2} U_{e,2} U_{\mu,3} U^*_{e,3} e^{-i(m_2^2 - m_3^2)L/2E}] \end{aligned} \tag{1.20}$$

and to equation 1.18

$$\begin{aligned} & |U^*_{\mu,1} U_{e,1}|^2 + |U^*_{\mu,2} U_{e,2}|^2 + |U^*_{\mu,3} U_{e,3}|^2 + 2Re[U^*_{\mu,1} U_{e,1} U_{\mu,2} U^*_{e,2}] \\ & \qquad + Re[U^*_{\mu,1} U_{e,1} U_{\mu,3} U^*_{e,3}] + 2Re[U^*_{\mu,2} U_{e,2} U_{\mu,3} U^*_{e,3}] = 0. \end{aligned} \tag{1.21}$$

Now subtract 1.21 from 1.20. We obtain an expression for the anti muon neutrino appearance probability.

$$P(\bar{\nu}_e \to \bar{\nu}_\mu) = 2Re[U^*_{\mu,1}U_{e,1}U_{\mu,2}U^*_{e,2}(e^{-i(m_1^2-m_2^2)L/2E}-1)]+$$
$$2Re[U^*_{\mu,1}U_{e,1}U_{\mu,3}U^*_{e,3}(e^{-i(m_1^2-m_3^2)L/2E}-1)]+2Re[U^*_{\mu,2}U_{e,2}U_{\mu,3}U^*_{e,3}(e^{-i(m_2^2-m_3^2)L/2E}-1)] \quad (1.22)$$

Would could follow a similar process to compute the probability that the initial electron antineutrino will interact again as an electron antineutrino.

$$P(\bar{\nu}_e \to \bar{\nu}_e) = \langle \bar{\nu}_e|\psi(L)\rangle =$$
$$1+2|U_{e,1}|^2|U_{e,2}|^2Re[e^{-i(m_1^2-m_2^2)L/2E}-1]+2|U_{e,1}|^2|U_{e,3}|^2Re[e^{-i(m_1^2-m_3^2)L/2E}-1]$$
$$+2|U_{e,2}|^2|U_{e,3}|^2Re[e^{-i(m_2^2-m_3^2)L/2E}-1] \quad (1.23)$$

The form of this expression allows us to apply the algebraic simplifications

$$Re[e^{-i(m_i^2-m_j^2)L/2E}-1] = Re[e^{i(m_j^2-m_i^2)L/2E}-1] =$$
$$\cos\left((m_j^2-m_i^2)L/2E\right)-1 = -2\sin^2\left((m_j^2-m_i^2)L/4E\right) \quad (1.24)$$

And rewrite the anti electron neutrino "survival probability."

$$P(\bar{\nu}_e \to \bar{\nu}_e) = \langle \bar{\nu}_e|\psi(L)\rangle = 1-4|U_{e,1}|^2|U_{e,2}|^2\sin^2\left((m_2^2-m_1^2)L/4E\right)$$
$$-|U_{e,1}|^2|U_{e,3}|^2\sin^2\left((m_3^2-m_1^2)L/4E\right)-|U_{e,2}|^2|U_{e,3}|^2\sin^2\left((m_3^2-m_2^2)L/4E\right) \quad (1.25)$$

By now it is explicitly clear that the appearance, disappearance and survival probabilities are all sums of three sinusoidal functions controlled by the mass differences of the energy eigenstates.

Obviously $m_3^2 - m_1^2 = (m_3^2 - m_2^2) + (m_2^2 - m_1^2)$ which means only two mass differences are independent. These two values, along with the three angles of the U_{PMNS} rotation matrix and the single complex phase δ totally determine everything that we can measure. The example given earlier was for $P(\bar{\nu}_e \to \bar{\nu}_\mu)$. Let's examine the (time) reverse of this process: the appearance of anti electron neutrinos from a beam of initially anti muon neutrinos. This is the phenomenon which will be the focus of DUNE. We could repeat the procedure outlined above.

$$|\psi(0)\rangle = \sum_k^3 U_{\mu,i} |\nu_i\rangle = U_{\mu,1} |\nu_1\rangle + U_{\mu,2} |\nu_2\rangle + U_{\mu,3} |\nu_3\rangle \tag{1.26}$$

The time and spatial dependence of the mass states is the same as before. We can therefore write an expression for $\psi(L)$.

$$|\psi(L)\rangle = \sum_k^3 U_{\mu,k} |\nu_k\rangle \, e^{im_k^2 L/2E} \tag{1.27}$$

So the probability of measuring an anti electron neutrino in this state is given by:

$$P(\bar{\nu}_\mu \to \bar{\nu}_e) = |\langle \bar{\nu}_e | \psi(L) \rangle|^2 = \left| (U_{e,1}^* U_{\mu,1} e^{im_1^2 L/2E} + U_{e,2}^* U_{\mu,2} e^{im_2^2 L/2E} + U_{e,3}^* U_{\mu,3} e^{im_3^2 L/2E}) \right|^2 \tag{1.28}$$

Which is almost the same as the probability as equation 1.17, except we take the complex conjugate of all of the contributing matrix elements, $U_{\alpha,k}$. Since these are just scalars, we can follow all of the steps we did previously. This way we obtain an expression analogous to equation 1.22 where the oscillations due to the different mass eigenstates is more explicit.

$$\begin{aligned} P(\bar{\nu}_\mu \to \bar{\nu}_e) = {} & 2Re[U_{e,1}^* U_{\mu,1} U_{e,2} U_{\mu,2}^* (e^{-i(m_1^2 - m_2^2)L/2E} - 1)] + \\ & 2Re[U_{e,1}^* U_{\mu,1} U_{e,3} U_{e,3}^* (e^{-i(m_1^2 - m_3^2)L/2E} - 1)] + 2Re[U_{e,2}^* U_{\mu,2} U_{e,3} U_{\mu,3}^* (e^{-i(m_2^2 - m_3^2)L/2E} - 1)] \end{aligned} \tag{1.29}$$

Of course Fermilab will also be searching for appearance of electron neutrinos from a beam of muon neutrinos (non antimatter). $P(\nu_\mu \to \nu_e)$ can be easily computed by simply taking the

complex conjugate of all of the contributing matrix elements $U_{\alpha,k}$ in the expression equation 1.29. This is true because neutrino spinors flavor states are the adjoints of antineutrino spinor flavor states.

$$P(\bar{\nu}_\mu \to \bar{\nu}_e) = 2Re[U_{e,1}U^*_{\mu,1}U^*_{e,2}U_{\mu,2}(e^{-i(m_1^2-m_2^2)L/2E} - 1)]$$
$$2Re[U_{e,1}U^*_{\mu,1}U^*_{e,3}U_{e,3}(e^{-i(m_1^2-m_3^2)L/2E} - 1)] + 2Re[U_{e,2}U^*_{\mu,2}U^*_{e,3}U_{\mu,3}(e^{-i(m_2^2-m_3^2)L/2E} - 1)] \quad (1.30)$$

Comparing the three analogous equations 1.22, 1.29, and 1.30 reveal the beautiful nature in which neutrinos physics obeys and breaks symmetries. If we apply a charge-parity (CP) reversal operation on 1.30, we get 1.29. Clearly neutrino oscillations will violate CP symmetry if $\delta \neq 0$ because the e^{id} phase appears only in the $U_{\mu,1}, U_{\mu,2}, U_{e,3}$ elements (refer to the PMNS matrix, equation 1.8). If we go on to apply a time reversal (T) operation on 1.29 then instead of looking at $\bar{\nu}_\mu \to \bar{\nu}_e$ we are considering the reverse process which is obviously $P(\bar{\nu}_e \to \bar{\nu}_\mu)$. But the probability for this interaction is what was computed originally in 1.22. We see that the time symmetry is violated again when $\delta \neq 0$ because of the phase which appears only in $U_{\mu,1}, U_{\mu,2}, U_{e,3}$. Now applying a T operation on $\bar{\nu}_\mu \to \bar{\nu}_e$ is equivalent to applying a CPT operation on $\nu_\mu \to \nu_e$. What we find is that $P(\nu_\mu \to \nu_e) = P(\bar{\nu}_e \to \bar{\nu}_\mu)$. In other words CPT symmetry is absolutely conserved in these processes.

1.5 Recent and Future Neutrino Physics

The initial example given here of the anti electron neutrino survival probability was the basis of several reactor experiments. One example is Daya Bay whose detectors were placed only a few km away to optimize a measurement of θ_{13}. Another was the KamLAND experiment, whose detectors were a few hundred km away to optimize The measurement of $(m_2^2 - m_1^2)$ as well as measure θ_{12} [8]. θ_{23} may be measured in a similar way or using solar or atmospheric neutrino experiments. Likewise a next generation reactor experiment called JUNO is exactly 53 km from two large nuclear power plants. It is optimized to measure θ_{13}, θ_{12}, $(m_2^2 - m_1^2)$ simultaneously and

precisely [9]. These distances are chosen with consideration of the antineutrino energy spectrum such that they optimize the amount of oscillation for a given mass difference based on the value L/E which appears in all of the expressions for survival and oscillation probability given in this section. DUNE will be able to utilize its large baseline, $L = 1300\ km$ and also control the E based on the output of its beam. This will allow it to probe parameter spaces not possible by any existing experiment.

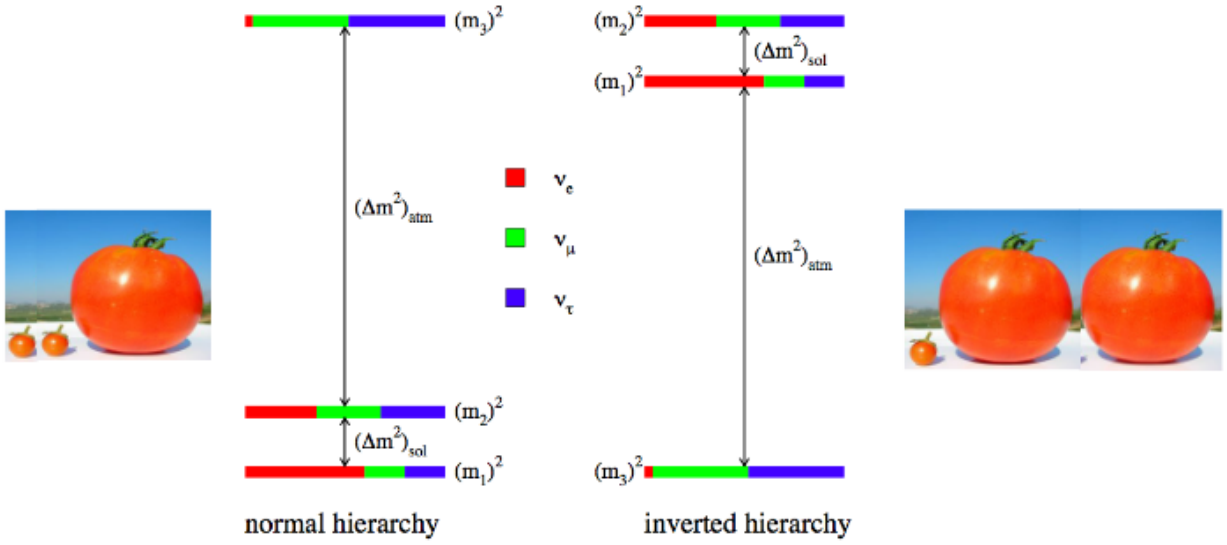

FIGURE 1.2: This cartoon illustrates the hierarchy problem. By studying oscillations, we know the two mass splittings of the neutrino energy states. One is significantly larger than the other. It is more difficult to know how to order them. Do we have two "big" masses and a much smaller one (normal hierchy), or two small neutrino masses and a much larger one (inverted hierarchy)? [10]

The sun is also a nuclear reactor which emits neutrinos with characteristic energies and directionality. Because knowing E and L allows solar neutrinos experiments to measure neutrino parameters.

Another option is to use look for the decay neutrinos from cosmic rays interacting with the Earth's upper atmosphere.

Lastly of course, it is possible to produce ν_e and ν_μ in particle accelerators like the one at Fermilab. The beam can be tuned to some range of energies and the detectors can be placed at desired

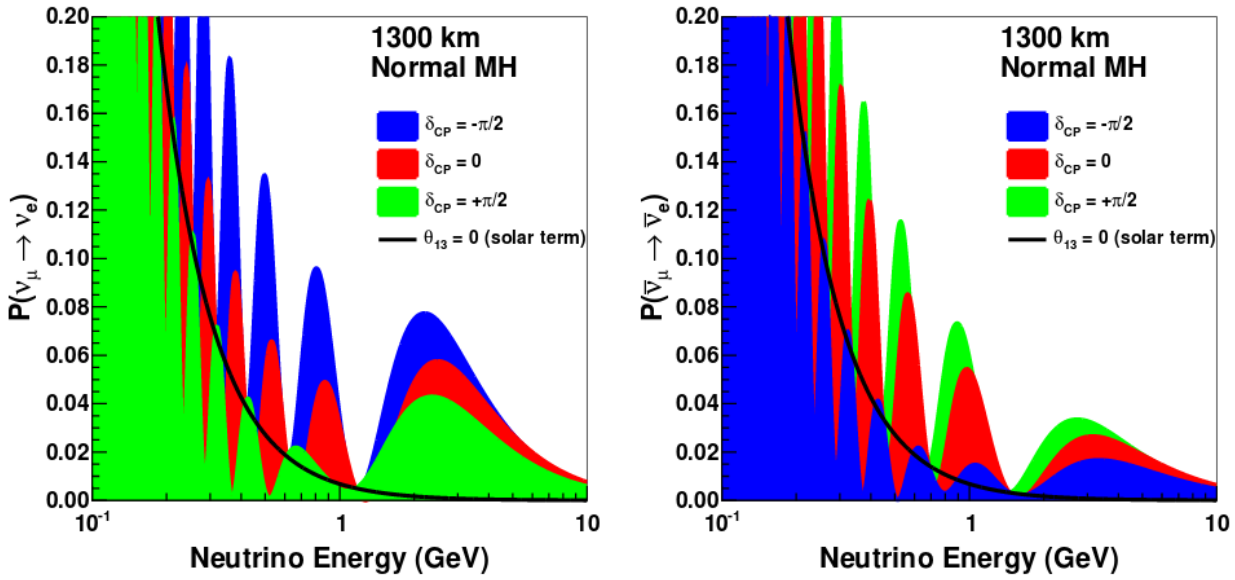

FIGURE 1.3: This plot illustrates the electron appearance probabilities for DUNE. This is the probability of a neutrino produced as either as a ν_μ (left) or as a $\bar{\nu}_\mu$ (right) to appear as ν_e (left) or as a $\bar{\nu}_e$ (right) after traveling L = 1300km from Fermilab in Batavia, Illinois to SURF in Lead, South Dakota through the earth. The probability depends on the energy of the neutrino, as was derived in equation 1.29 and 1.30. Crucially, it will also on the CP violating phase δ, which is contained in the $U_{\mu,1}, U_{\mu,2}, U_{e,3}$ factors in the same equations. [1]

distances L so to optimize measurements of mass differences and mixing angles. Fermilab alone has hosted several experiments with L a few hundred meters, as well as MINOS whose detectors were built underground in Minnesota 735 km away and NOvA, which is currently taking data and located 804 km away. Construction has already begun on the DUNE site which will be hosted at SURF, the former Homestake Mine in Lead, South Dakota, located 1300 km from Fermilab.

The various data from the reactor, solar, atmospheric, and beam neutrino experiments has been complementary and somewhat consistent. Currently all of the mass differences and U_{PMNS} rotation angles are known with varying levels of precision. Current experiments, NOvA and T2K in Japan are attempting to measure the imaginary phase δ. DUNE will be able to measure δ as well as all of the other mixing angles with unprecedented precision. It was assumed in our derivations in the previous section that there were exactly three neutrino states. There is some experimental and theoretical motivation to suggest this may not be true. If indeed there are more than three neutrino states, then the PMNS matrix will not be unitary. DUNE may have adequate precision capabilities to measure this and possible discover more neutrinos beyond the three which are currently known.

Furthermore, though previous neutrino mixing studies have measured the the mass differences, they have not been able to decisively resolve whether these mass states exist in the so called "normal hierarchy" or in an "inverted hierarchy." We know the mass differences $m_1^2 - m_2^2 \approx 8 \times 10^{-5} eV$ and $|m_3^2 - m_2^2| \approx 2 \times 10^{-3} eV$, but we do not know if $m_3 > m_2 > m_1$ (corresponding to normal hierarchy) or if $m_2 > m_1 > m_3$ (corresponding to inverted hierarchy) [8]. In other words we need to know the sign of $m_3^2 - m_2^2$. This problem is illustrated schematically in the cartoon shown in figure 1.2.

1.6 Proton Decay

The reality is that it is incredibly difficult to measure the interactions of neutrinos with nuclei. To build a neutrino detector you must therefore increase the chance of interacting with a single neutrino by building massive, gigantic detectors. The size of the proposed DUNE experiment will be discussed in more detail in the next chapter. For now it suffices that having a huge volume

of nuclei constantly being recorded by sensors allows you to detect (or more likely constrain the rates of) other extremely rare processes. Most important of these is proton decay. The existence of proton decay is theorized by several GUTs. Observing it would be an indirect measure of the structure of the universe at some of the highest imaginable energies.

1.7 History of Supernova Physics

The history of supernovae is ancient. For a long as there have been written records, there have been reports of "new" or "guest" stars. These appear very bright, persist for a few weeks, and then become dimmer until they appear as a normal star or disappear from the sky. The most ancient reports of these events tends to be associated with epic lore and not credible. There are around eight generally accepted supernovae which were visible to the naked eye during the last two millenia. In 185, 386, 393, [12] 1006, 1054 (leaving the Crab nebula illustrated in figure 1.4), 1181, 1572 (Tycho's supernova), 1604 (Kepler's Supernova) and 1685 [13]. Some of these naked eye supernovae cast shadows during their peak luminosity and were as bright as the moon for weeks before disappearing. They are surely magnificent to behold and it is perhaps no coincidence that there were two such events during a span of thirty-two years which included the lives of Brahe, Galileo and Kepler.

Though the history of supernovae is ancient, the history of our physical explanations for them is recent. It probably begins where the history of neutrinos begins, with the discovery of radioactivity in the 1890's. In 1905 Einstein's theory of relativity opened the door for mass-energy equivalence. Precision measurements of hydrogen and helium mass showed that Helium is just less than four times the mass of helium prompting the astronomer Arthur Eddington to suggest the the transmutation of four hydrogen atoms to helium may be the source of the sun's energy in 1920. This was a totally speculative suggestion especially given that it predated the discovery of the neutron by a decade. However Eddington's intuition turned out to be correct. In 1930, the legendary Subrahmanyan Chandrasekhar, aged 20, combined quantum statistics with special relativity and to correctly calculate what is now called the Chandrasekhar limit [13]. This limit represents the maximum mass a star can have to maintain itself as a white dwarf. Any star larger

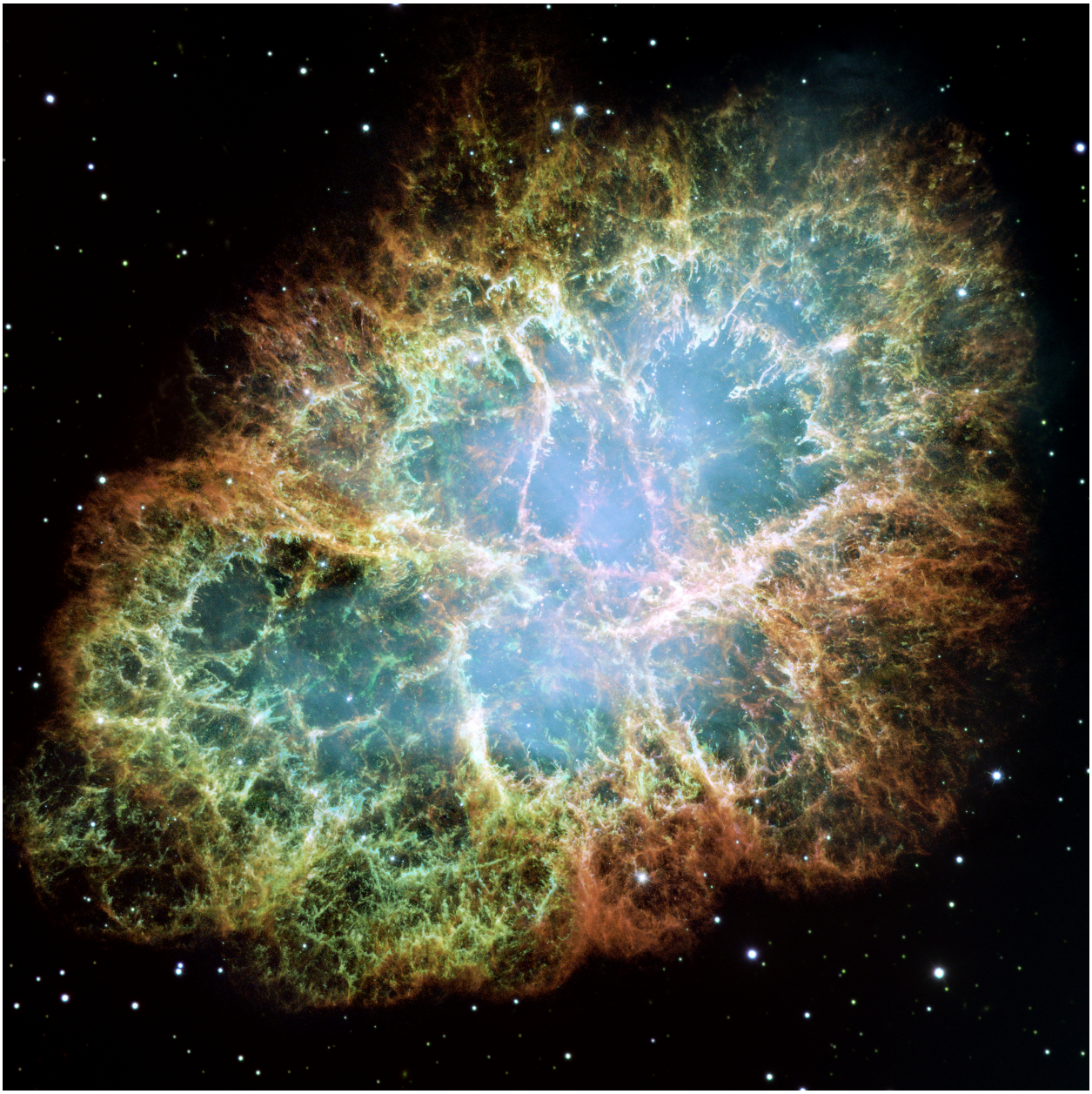

FIGURE 1.4: An image of the Crab Nebula. It appears to the naked eye like a dim star located in the Taurus constellation. The position, time, and brightness of this former supernova were independently recorded by Arab and Chinese astonomers in 1054. It remains a relatively bright object in the sky due to its proximity to Earth. The orange matter are gas debris of the outerlayers of the former red giant star. They span over 5 light years in space. The blue glow is due to the neutron star's magnetic field interacting with electrons in the diffuse gas. The neutron star itself is too small and too dim to be seen directly, but its rotation can be measured by the pulses of radiation it emits as jets. [11]

than about 1.4 times the mass of the sun will collapse. In 1932 the neutron was discovered by Chadwick. In 1934 Walter Baade and Fritz Zwinky make another speculative and generally true suggestion: that supernovae represent a transition of large stars to neutron stars releasing huge amounts of energy in the process. They coined both the term supernova and neutron star. The same year, Fermi published his theory of beta decay. The reverse of this process is what is involved in turning protons into neutrons. In 1938 Lev Landau calculated that at extreme densities, nuclear configurations of pure neutrons are energetically favorable to "normal" nuclei. Oppenheimer built off of Landau's studies to establish an upper limit on neutron star masses before they too collapse (presumably into either into a black hole or an extremely dense, strange object).

Finally in 1939 Chandraskar puts all the pieces together and expresses what is essentially our current understanding of supernovae. They are created when the electron degeneracy pressure is not strong enough to support the mass of a star. The electrons are forced into the nuclei via inverse beta decay. This will produce an insane amount of neutrinos. These are the only particles that are weakly interacting enough to carry off most of the energy released during the gravitational collapse. The core essentially becomes a dense ball of neutrons called a neutron star. The outer layers "bounce" off of the neutron star and are blown outwards.

During the neutronization of the stellar core, an enormous flux of neutrinos is produced. When neutrino detectors became viable it was proposed that should a supernova occur close enough to the Earth, the detectors would be sensitive to them. In 1987 just such a supernova occurred, as mentioned in section 1.3. The Kamiokande II experiment measured 12 events, the IMB experiment measured 8, and Baksan measured 5 in a simultaneous period of only a few seconds. Just a few hours later a supernova burst was observed 168,000 light years away in Large Magellanic Cloud dwarf galaxy.

1.8 Supernova Physics

Supernova are of great importance because they are one of the primary processes that fuse together the heaviest elements in the universe (which our Earth and ourselves are made from) and they additionally have a built in mechanism to disperse these elements into deep space.

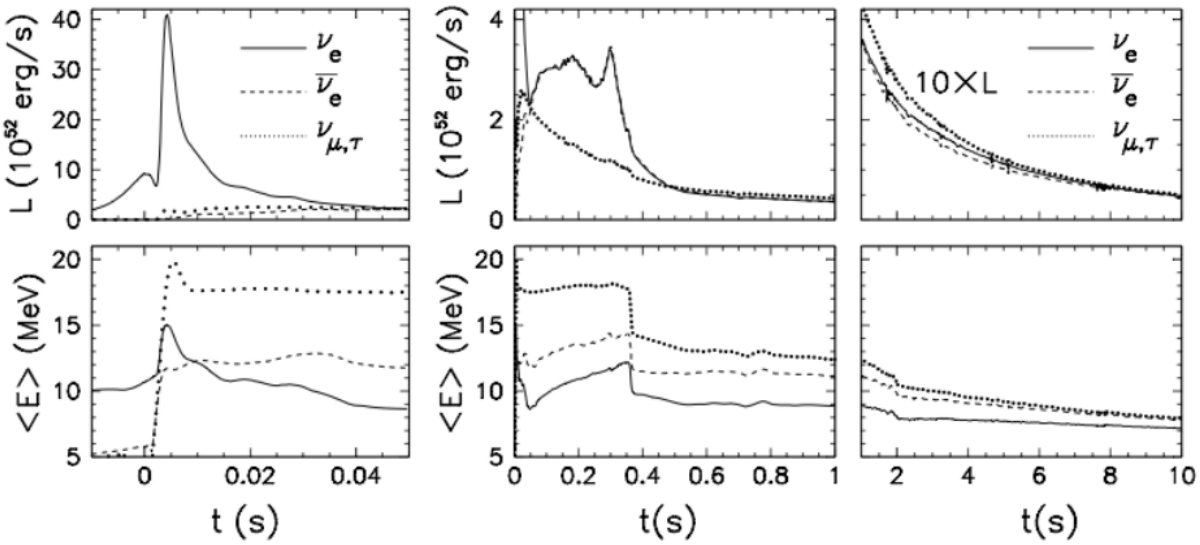

FIGURE 1.5: This figure illsustrates the production of neutrinos from within a supernova. The top plots illustrate the evolution of the luminosity over the stages of neutronization, accretion, and cooling. The bottom plots illustrate the average energy per neutrino produced over these same time frames. [14]

The exact sequence of events just before the neutronization is not clear. Are the iron nuclei of the core destroyed in photonuclear processes prior to the inverse beta decays which turn the protons to neutrons? Likewise, the details of how the system evolves from a free fall collapse to an expanding acretion shockwave is still not settled. The energy that carries the outer layers into deep space is probably mostly due to induced nuclear reactions sparked during the initial collapse. There may be a significant shockwave effect in the outward going gas. The density of this shockwave has been hypothesized to vary in time due to hydrodynamic effects. In supernova literature these are refered to as standing accretion shock instability (SASI waves) [15]. The nuclear processes will be modulated by the intense flux of neutrinos coming from the core. For some period of time the star will be opaque even to the neutrinos. In this extreme scenario the neutrinos will be Pauli blocked (have few available quantum states to transition to) and behave like a Fermi sea analogous to the behavior of electrons in metals. Also due the the Pauli, blocking exotic Gamow-Teller reactions are expected to occur [16]. This region of matter which is opaque to the neutrinos is called a neutrinosphere in analogy to the photosphere of the sun [12]. Even

outside of this neutrinosphere there will be interesting effects. The neutrinos streaming out of the supernova will exist in such a density that their oscillations will be modulated not only by the matter of the dying star, but also by themselves! This will form a feedback loop which could probably not be formed in any other physical system. The shockwave, its time dependence, the high neutrino density effects will all produce a measurable signal on the DUNE detector. Also exciting is that part of the supernova signal is dependent on the mass ordering of the neutrinos, as illustrated in figure **??**. There may even be signatures related to neutrino magnetic moments. If other weakly interacting massive particles exists, they could interfere with the behavior of the neutrinos exiting this impressive system [1]. All of these signatures will have a time dependence. DUNE will be capable of time resolutions of roughly 500 ns, and is expected to have the capability to read out continuously for 30 seconds when it is triggered to go into supernova data acquisition mode. In this way the signals described above could be observed microsecond by microsecond! **The ability of DUNE to study the physics described above will depend on submicrosecond timing resolution which can only be provided by the photon detection system.**

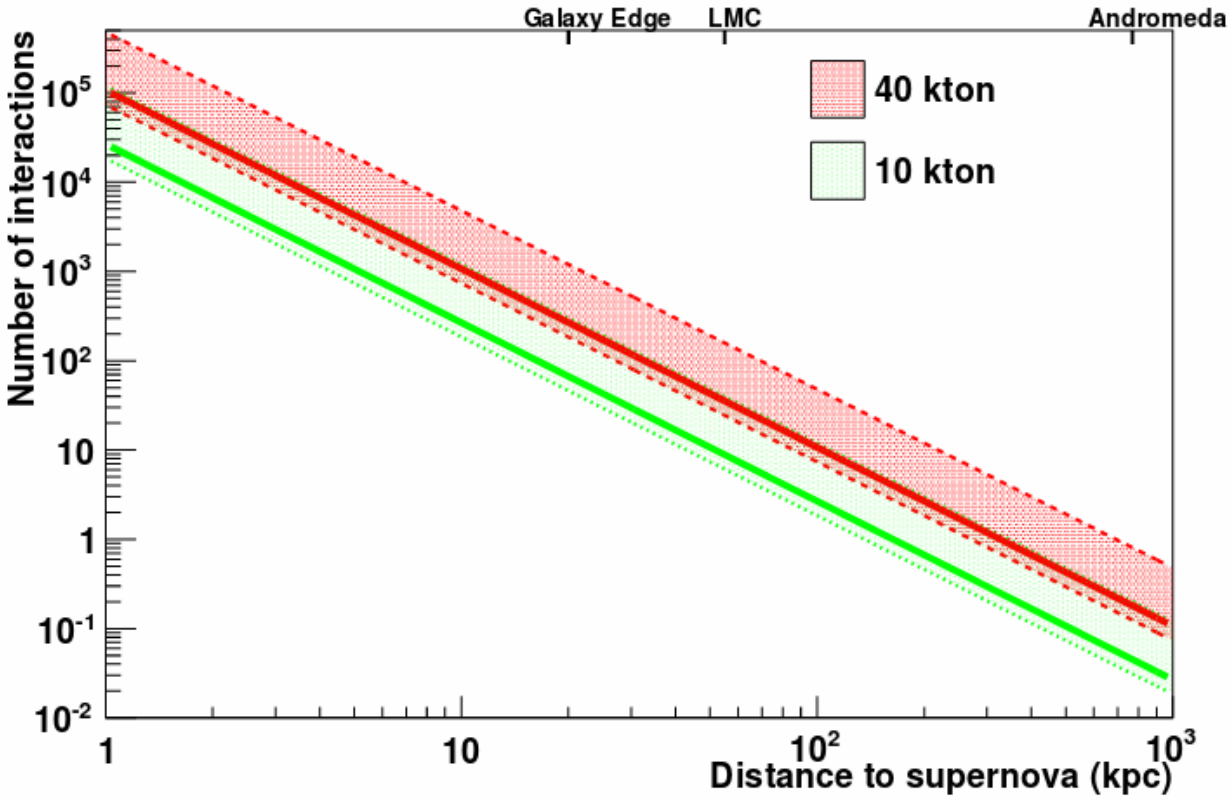

FIGURE 1.6: This illustrates the number of supernova neutrino interactions a 10kt and a 40kt liquid argon detector is expected to be sensative to. This number depends on the distance to the supernova illustrated here in kiloparsects (1 kpc = 3262 ly) [1]

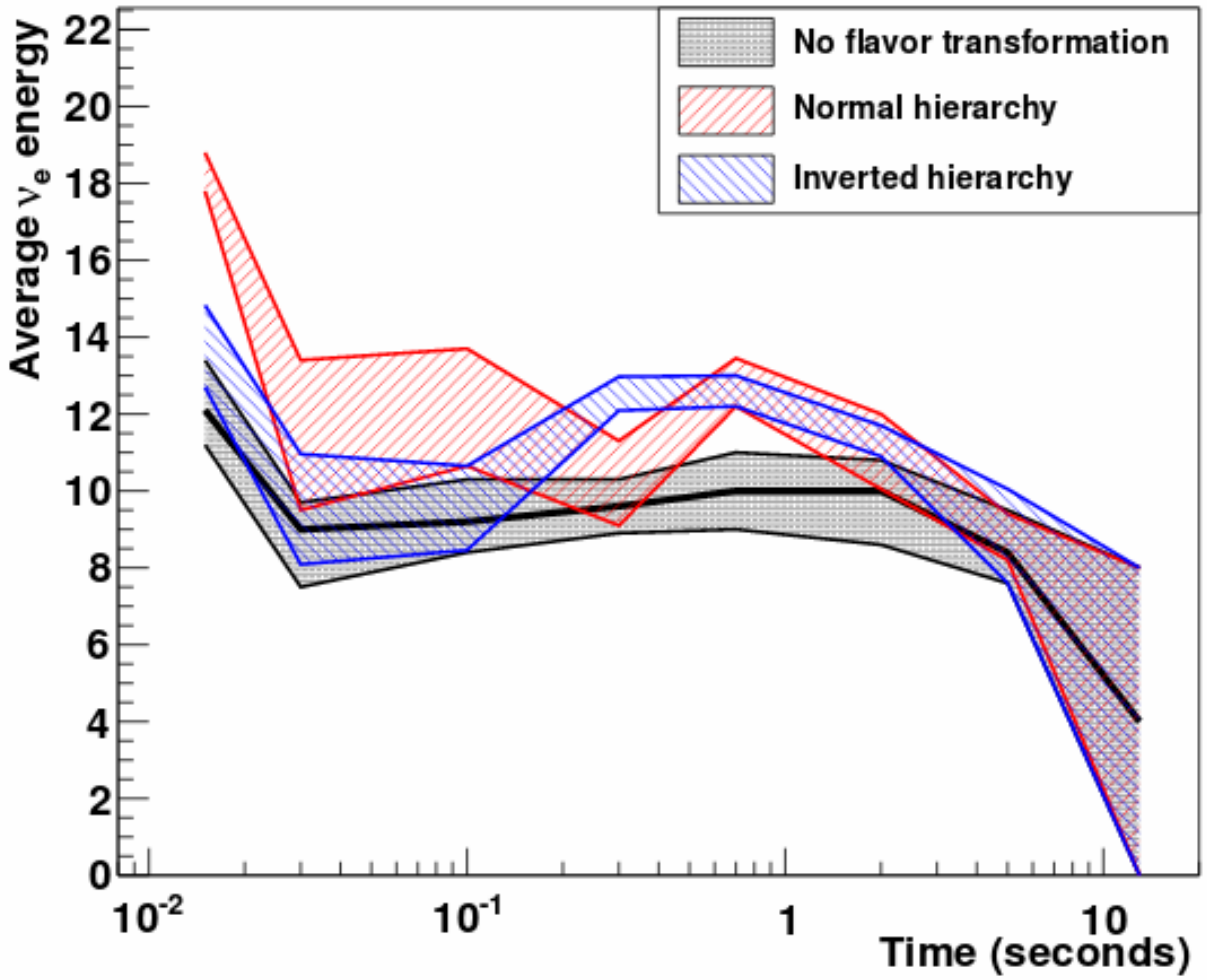

FIGURE 1.7: The average energy of ν_e is expected to vary rapidly on the time scales of fractions of a second. Exactly how this energy varies in time will depend on the precise mass ordering of the three neutrino states. [1]

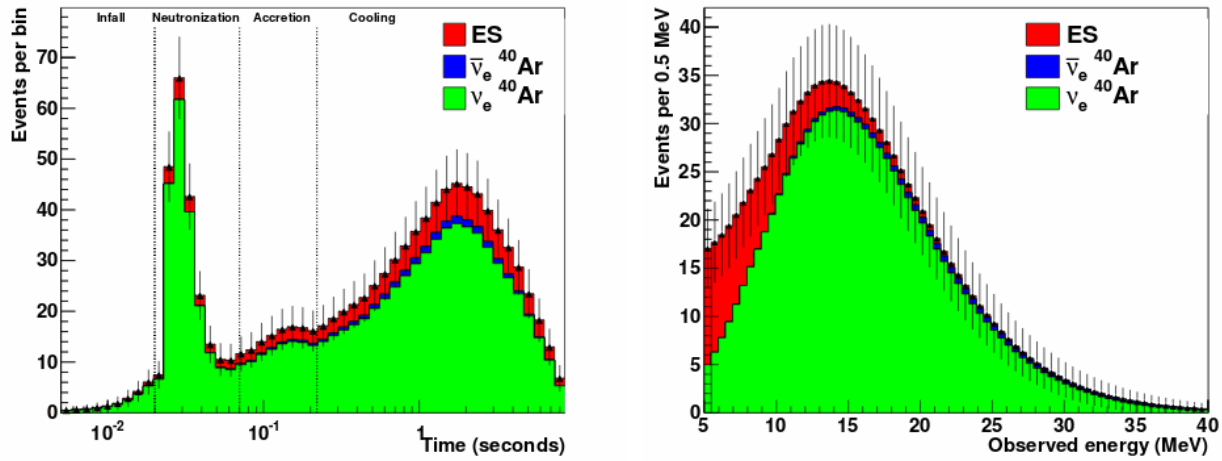

FIGURE 1.8: This figure illsustrates the expected types of signals that a 40 kt liquid argon detector would be able to record assuming that the supernova occured 10kpc (33,000 ly) away. ES = elastic scattering off of a nucleus or electron, $\bar{\nu}_e$ ^{40}Ar = inverse beta decay with an argon nucleus ν_e ^{40}Ar = beta decay with an argon nucleus. [1]

Chapter 2

DESCRIPTION OF PROTODUNE AND DUNE FAR DETECTORS

2.1 Introduction to Liquid Argon Time Projection Chambers (LArTPCs)

Liquid Argon Time Projection Chambers are attractive devices in neutrino physics. The large nuclei of argon, combined with the high density of the liquid mean that the cross sections for neutrino interactions are relatively high. When subjected to sufficient electric fields, the ions produced in particle interactions within the detector volume are drifted through the liquid at energies sufficient to excite $\mathcal{O}(10000)$ electrons per drift cm. The speed that these electrons drift towards the collection system can be well characterized as demonstrated in several previous and ongoing experiments including the LArIAT, CAPTAIN, and MicroBooNE [17]. The electrons will be drifted to a series of induction and collection wires. The currents produced on them can be converted into a digital signal and reconstructed with high position resolution in the plane parallel to the wire plane. Furthermore by measuring the earliest light produced in an interaction, the time between the light and the charge collection signals can be multiplied by the electron drift velocity to give spatial resolution perpendicular to the collection plane. Knowing the length of the tracks, position within the detector, and strength of the signal allows excellent energy reconstruction. The large gain and ability to accurately reconstruct positions, lengths, and energies of induced tracks allows LArTPCs to behave like digital bubble chambers.

The light signals are of particular importance to this thesis. An excited argon atom will naturally bond with a second argon atom and create a state similar to a Rydberg atom of two argon nuclei with a single shared electron. This excited state is called an eximer and can exist in singlet and triplet states. The deexitation of an excimer state in a LArTPC will generate $\mathcal{O}(10,000)$ photons per MeV with a characteristic wavelength of 128 nm. The energy required to form excimer states is sensitive to the separation distance of two atoms. The 128 nm light does not have enough energy to excite excimers of argon atoms with an average atomic spacing given by the temperature of the liquid. Because this 128 nm light is not the correct energy to excite any individual argon atoms, nor to stimulate excimer states, liquid argon has an impressively large attenuation length for its own scintillation light [18]. In fact the attenuation length is determined by trace impurities like nitrogen, oxygen and water in the liquid argon. The exact attenuation length can vary greatly depending on how much of these impurities is present, but tends to be $\mathcal{O}(10)$ m. [2]. This light can then be measured either by traditional photomultiplier tubes (PMTs) or, in the case of DUNE and ProtoDUNE, solid state silicon photomultipliers (SiPMs). It is possible to use this light to gain additional information about interactions within the drift volume by accurately measuring the precise number of photoelectrons (PEs) which cause cascades in the photodetectors. These devices in the context of ProtoDUNE are discussed in chapter 4. The primary challenges of detecting this light are the durability of SiPMs at cryogenic temperatures, discussed in chapter 4, as well as poor quantum efficiency of light detection of 128 nm light, discussed in chapter 3. These challenges can be overcome and the photon detection system (PDS) can offer valuable additional information on energies via PEs measured and offer information about the precise nature of various interactions via pulse shapes of the readout signals. Also, most significant to this thesis, light detectors are tools that offer timing information for interactions not stimulated by a neutrino beam like nucleon decay and supernova interactions. The usage of photon detectors in the context of supernova neutrino interactions which are discussed in some detail in chapter 5.

2.2 Description of the ProtoDUNE Detector

The ProtoDUNE detector is intended largely to demonstrate the feasability of scaling up the massive LArTPCs that are envisioned for the DUNE Far Detector. ProtoDUNE is the largest LArTPC built to date, containing a 0.77 kt mass of liquid Argon. It is housed at CERN and will measure interactions from a charged particle test-beam. ProtoDUNE itself is composed of individual modules which are intended to be a identical or nearly identical to modules that will be stacked together to form the future DUNE far-detector. The cryostat technology is adapted from industrial cryostats used in large scale liquified natural gas storage. [19] It is essentially a large cryostat in the shape of a rectangular block containing both the liquid argon, the charge and photon collection systems and associated electronics. It is 7 m long in the direction of the beam (z direction), 6 m tall (y direction), and 7.2 m wide in the drift direction (x direction). In the center are three cathode plane assemblies (CPAs) which are biased at -180 kV. The CPAs are flanked on either side in the x direction by the anode plane assemblies (APAs) with a small bias. This entire system is surrounded by a field cage to give field uniformity. This bias generates an electric field of 0.5 kV/cm whose direction defines the drift direction. Each APA section contains a charge readout and collection system (usually referred to as the TPC) consisting of three layers of wires. The first two layers are covered by an electrical insulator so that as ionization electrons drift past them they produce a dipolar induction signal. The last layer of wires is uncovered and collects electrons generating a monopole current signal.

These induction and collection wires are all oriented in three different directions. The timing of the signals on each of these differently-orientated wires can be deconvoluted to reconstruct where the charges must have originated in the volume prior to their drift towards the anode. The TPC system provides excellent spatial resolution in the vertical-beam-direction plane as the wire spacing is 4.75mm. In principle due to the three different orientations of the wires the TPC should be capable of reconstructing tracks in three dimensions. However having the light collection systems significantly improves the three dimensional reconstruction capabilities. In addition to the TPC system, each anode contains 10 photon detectors. These photon detectors are generally 2.1

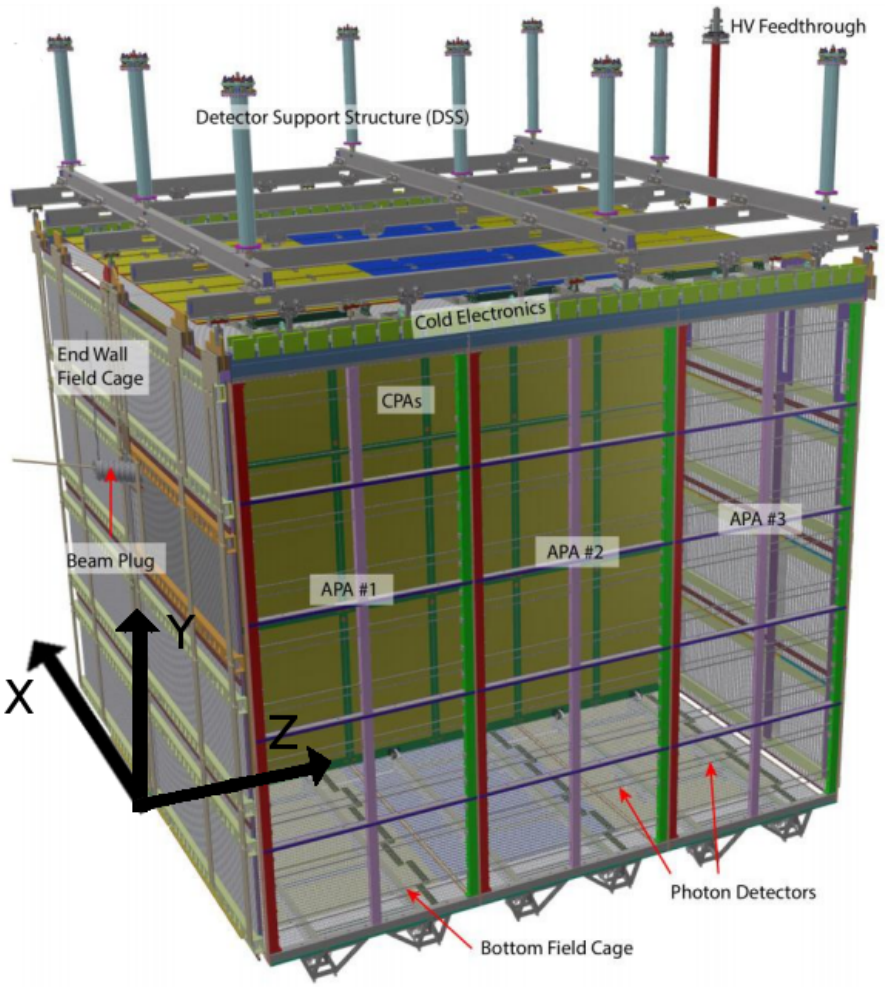

FIGURE 2.1: An illistration of the design of the protoDUNE cryostat. [19]

m long and 8.6 cm tall. These detectors generally consist of a wavelength shifter to convert the 128 nm liquid argon scintillation into 430 nm photons. Generally at the ends of each light guides are a set of 12 SiPMs which are sensitive to the 430 nm photons. This array of light detectors is called the photon detection system (PDS). The photon detection system is part of an ongoing R&D project with important implications for the future DUNE far detector. Highlights of the photon R&D effort are discussed in chapter 3.

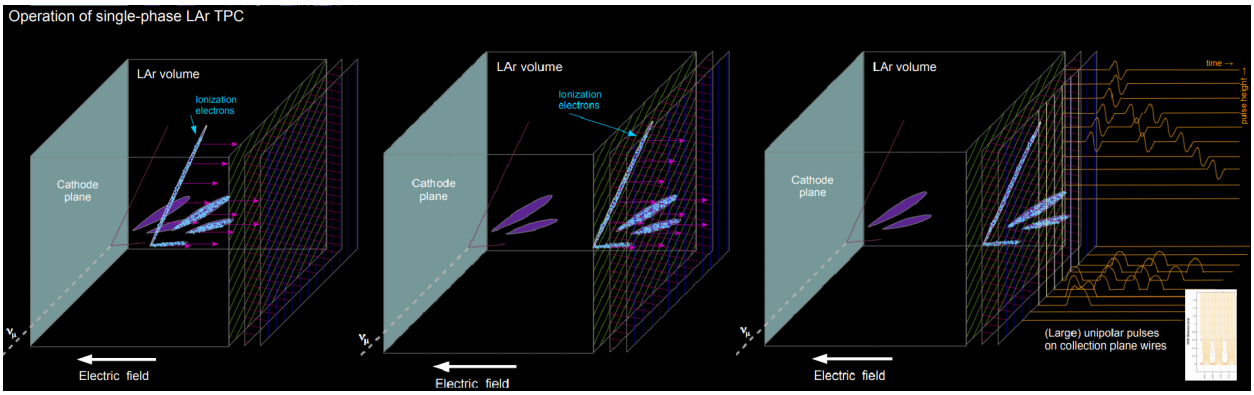

FIGURE 2.2: This cartoon illustrates how tracks and showers of ionization electrons, which are copiously produced by interactions of charged particles they particles move through the volume, will produce signal. The ionization electrons will be drifted through the detector space towards the APA plane. The amount of energy deposited is directly related to the number of ionized electrons. As the drifted electrons interact with the APAs, they will generate dipole signals on the induction wires and monopole signals on the collection wires. These wires are oriented in different ways such that it is possible to tell the position in y and z space of the drifted electrons by which wires produce signals coincidently.[20]

2.3 DUNE/LBNF Requirements and Implications for the Far Detector

The DUNE/LBNF science program is an audacious effort which will overcome significant constraints.

In order to properly test neutrino mixing, it is necessary for there to be a neutrino beam, a near detector to measure initial cross sections, and a far detector which is sufficiently far away for the mixings to be apparent. For the DUNE/LBNF program the beam production facility and

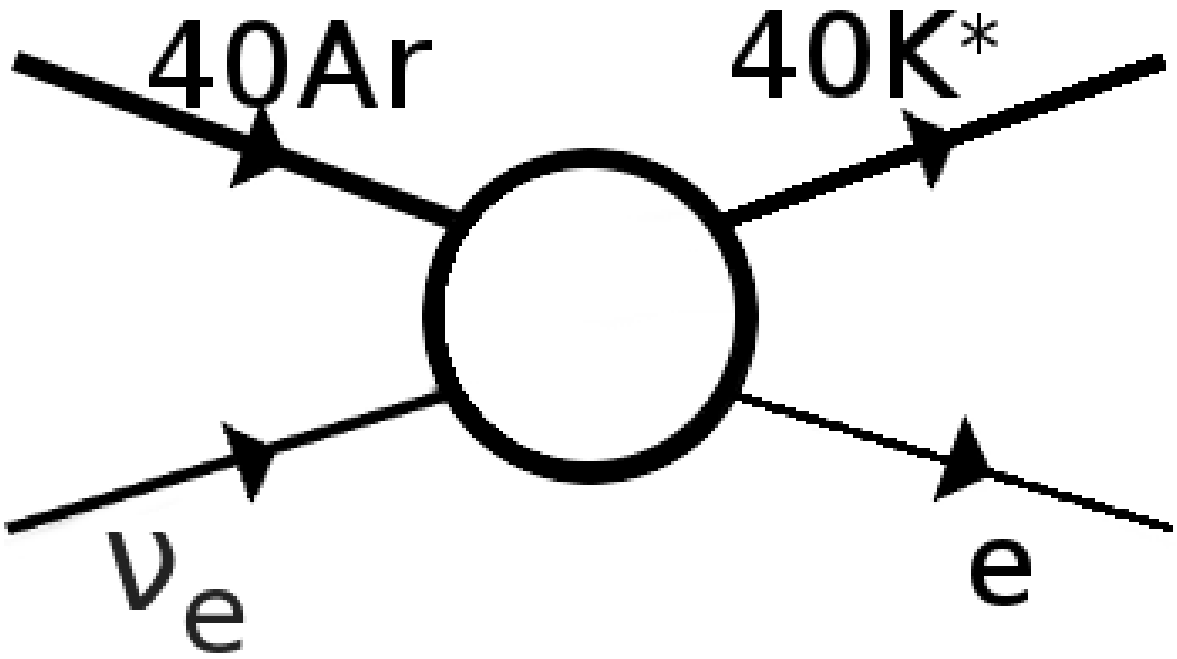

FIGURE 2.3: There are many signals that LArTPCs are capable of measuring. One of the most basic and most important for supernova physics in DUNE is the induced beta decay of 40Ar shown above. This interaction would produce at least single charged particle track via the outgoing electron. The deexcitation of the excited 40K nucleus may produce other signals.

near detector will be located on the Fermilab campus in Batavia, IL while the far detector will be located 1300 km away at the Sanford Underground Research Facility (SURF) in Lead, SD.

The neutrino beam will be a similar but more powerful version of the existing NuMI beam at Fermilab. Protons will be accelerated to a controlled energy, and then incident on a graphite target. The protons will interact with the target to form pions and kaons which decay in flight. The decays of these particles will create the neutrinos that comprise the beam incident on the near and far detectors. When the pions and kaons decay, there is an unavoidable angular distribution in the outgoing neutrinos. The neutrino beam produced at Fermilab will really be a cone of neutrinos which spreads out the farther they are from Batavia, Illinois. By the time they reach Lead, South Dakota the beam flux will be greatly diminished.

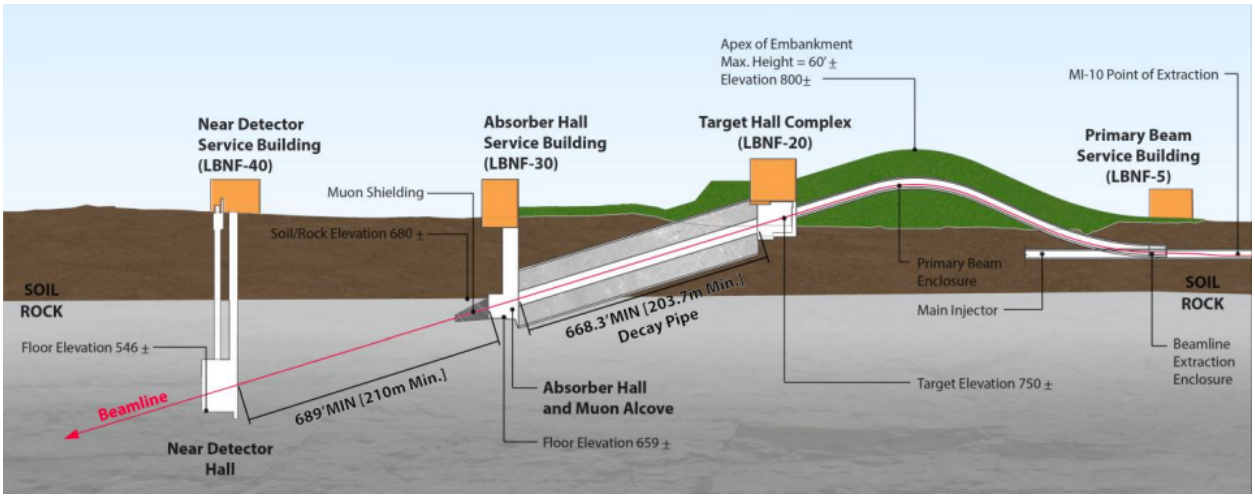

FIGURE 2.4: An illistration of the LBNF [21]

In order to precisely measure the different species of neutrino interactions, it is necessary to block out other types of signals which otherwise would dominate the rare beam interactions. For this reason both the near and far detector will be underground. The rock above the detectors shields them to the cosmic rays produced copiously in our own atmosphere. This need of shielding is particularly important in the case of the far detector where the flux is diminished. In fact, from a beam of 10^{21} protons on target per year at Fermilab, there will only be a few hundred neutrino interactions per kton per year in the DUNE far detector [22]. Most of these interactions are

charged current interactions with muon neutrinos.

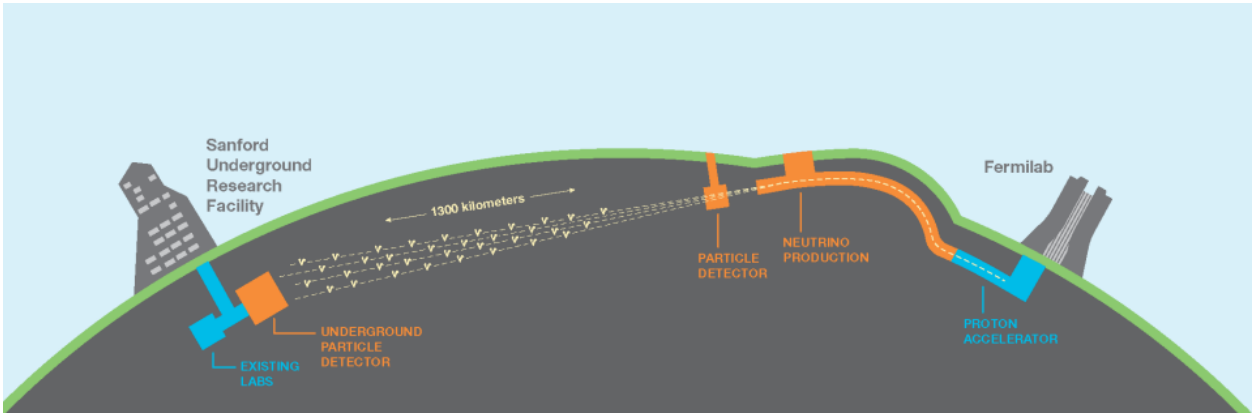

FIGURE 2.5: A Cartoon of the LBNF and the DUNE Far Detector including the beam line, decay path and near detector. [1]

Because neutrinos interact so rarely with matter, neutrino detectors need to have a large mass in order to have a chance to interact with a tiny fraction of incident particles. Again, this is a particularly large constraint for the far detector which will receive a vastly diminished neutrino flux.

The SURF facility is 1300 km from Fermilab, deep underground (approximately one mile), and has the correct geology for the construction of an underground cavern large enough to service the needs of the far detector.

2.4 Description of the DUNE Far Detector

The DUNE far detector will consist of four 10kT fiducial volumes housed in identical cryostats. These volumes are scheduled to be constructed individually with different technologies as they develop.

The first 10kt module will be made up of an array of CPA and APA modules similar to the ProtoDUNE configuration described in section 2.2 but in a larger quantity. It will have a central APA flanked on either side by CPAs flanked on either side with two more APAs. The central APA will be able to measure the 3.6 m drifts on both sides of it. This arangement will be 2 APAs high

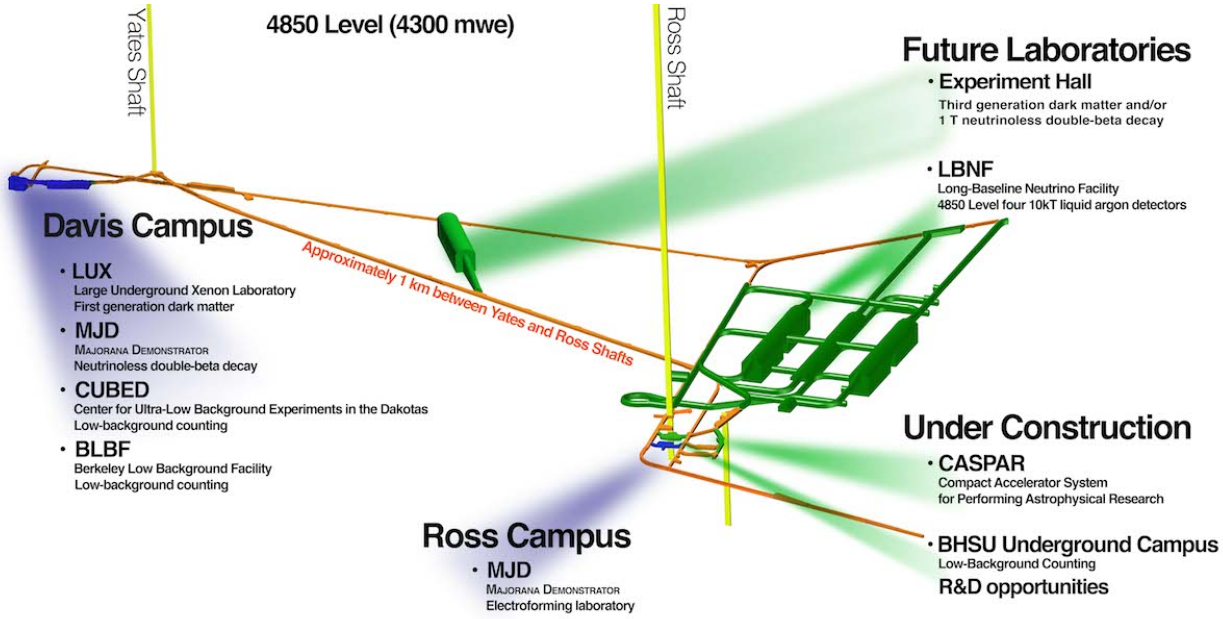

FIGURE 2.6: A map of the 4850 foot level of the SURF facility [21]

and 25 APAs long. All told this detector would then be about 21.6 m wide by 12 m tall by 58 m long. [23]

The first 10kt module will be a single-phase LArTPC, in the sense that it will use only argon in the liquid phase. Other attractive designs of LArTPCs have a dual-phase design where electrons are drifted out of liquid into gaseous argon before being detected. These designs improve signal and are under rapid research and development for possible implementation in one of DUNE's later 10kt modules.

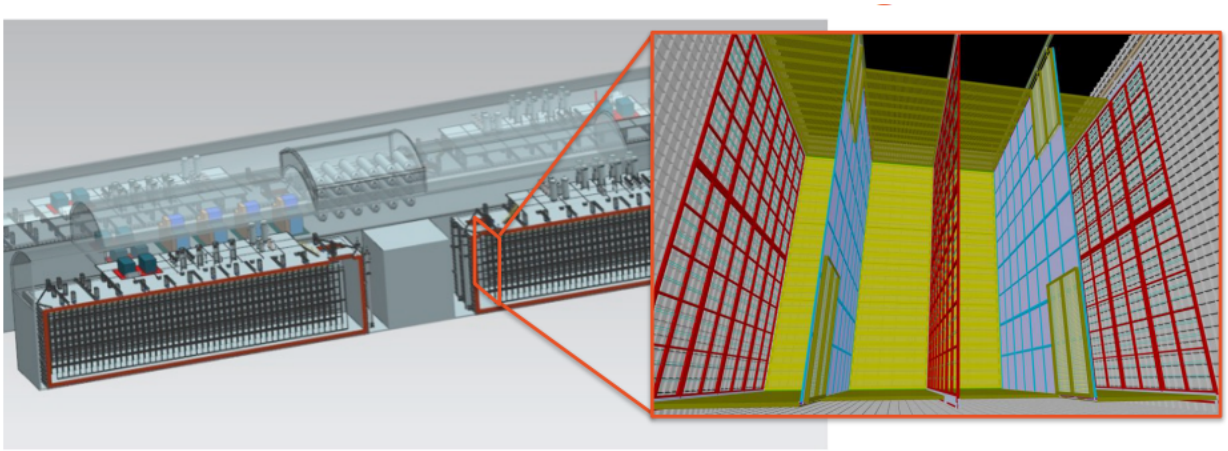

FIGURE 2.7: An illustration of the geometry of the first 10kt module of the far detector. APA planes are shown in red, CPA planes in blue. [21]

Chapter 3

PHOTON DETECTION SYSTEMS

3.1 Introduction

The photon detection system (PDS) is a critically important system within DUNE. It is especially important for measurements that cannot be time correlated with neutrinos produced at Fermilab. Most important to this paper are events that originate from supernovae. The charge detectors of the TPC are effective in reconstructing an event in two spatial dimensions. However due to space charge and drift effects, they struggle with resolution in the direction perpendicular to the APA plane (x direction). Also because of the large drift volume, they are not able to effectively reconstruct the initial time, T0, of an interaction. The time resolution of the PDS by contrast is excellent, generally within a few hundred nanoseconds. This is because light reaches the detectors essentially instantaneously. Furthermore, by measuring the time between the light signal and the charge signal, it is possible to reconstruct how far the charge must have drifted and thereby reconstruct x position. This process is discussed in the context of supernovae events in more detail in chapter 5.

This chapter introduces several challenges related to designing the PDS. It briefly discusses concepts in detector technology which address some of these challenges and offers a brief summary of the leading designs for such a system which will soon be taking data in ProtoDUNE. Similar but improved systems will be used in the DUNE Far Detector. Some potential improvements are discussed at the end of this chapter.

3.2 Basic Principles (and Challenges)

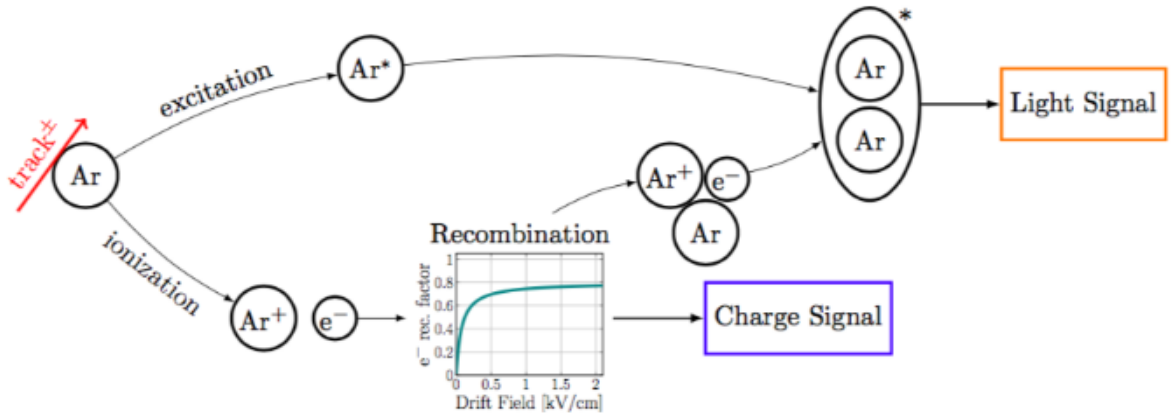

FIGURE 3.1: This diagram illustrates the various processes relevant to the PDS in DUNE. [2]

The process which creates scintillation light was discussed briefly in chapter 2, but it is worth discussing again before discussing the designs themselves. Excited argon atoms tend to form eximers. These eximers can exist in either singlet or triplet atomic states. In the presence of the 500 V/cm electric field in the DUNE detector volume, the decay of these eximer states release 24,000 photons/MeV. The wavelength of light produced in these decays is the same regardless of whether the excited state is singlet or triplet. The light is within a 10 nm band centered around the characteristic scintillation peak of 128nm. The time it takes for the eximers to decay is characterized by the time constant which does depend on the eximer state. The prompt or short time constant corresponds to the singlet state and is $\tau_{prompt} = 7ns$. The long or late time constant corresponds to the triplet state and is measured to be $\tau_{late} = 1.3\mu s$. The probability for the argon to form a singlet versus a triplet state is related to what particle is depositing energy into the liquid argon. This fact may later be used for particle identification using only the light signals [24].

The challenges faced by any photon detection system suitable for a future single phase DUNE Far Detector are many. It should have high overall detection efficiency while keeping this efficiency as uniform as possible throughout the volume. Covering such a large volume requires

many sensors which means that cost is a constraint. The system will need to detect scintillation light of about 128 nm which is lower than what most current SiPMs are designed to detect. They will be bathed in liquid argon and will thus need to be durable enough to operate at the extreme temperature of -186 C. The system must be able to take extremely accurate measurements of the number of PEs in a signal and preferably be capable of pulse shape analysis. The system must not only operate at a high gain to detect the faintest signals possible, but also must operate at a low noise in order to ensure that data comes in at a manageable rate. The PDS must fit in the APA modules in the limited space behind the wire planes (which will block a significant fraction of the light). For the APAs along the central plane of DUNE, the photon detection system will need to record light signals for the two drift volumes on either side of the plane. The time resolution is somewhat complicated by the fact that there are two time constants related to the deexitation of eximer states. Its further complicated by the fact that at 128nm, the index of refraction of liquid argon changes significantly with wavelength, so even for the narrow 10 nm band of light, there will be dispersion effects. Time resolution in the context of supernovae is discussed in 5, and we will see that for this purpose the time resolution of the PDS is more than adequate for most designs.

Most SiPMs available on the market are only $\mathcal{O}(10s)$ mm^2. Since the protoDUNE and DUNE APAs are several meters tall and wide, this puts significant limitations on the geometric efficiency that is possible. One strategy to overcome this is to use large light guides. Two of the designs that will be discussed in section 3.3 rely on 210 cm by 8.6 cm light guides coupled to SiPMs. However challenges still remain. The optimal wavelength to transport light may be different from the SiPM's optimal wavelength for detection (and neither of these is 128 nm). To address this challenge, wavelength shifters are added to the designs. These are generally made of tetraphenyl butadienne (TPB) coating significantly reduces the light signal [2] and may be prone to dissolving into the liquid argon. Furthermore, these guides still have huge inefficiencies in the transportation of a photon from one part of the guide to the SiPMs coupled to the end. This is because light transport is mediated either by fluorescent scintillation or by total internal reflection. Of course total internal reflection is only effective for a small range of angles with respect to the light guide surface. Another strategy is to use filters to both shift the photon wavelength and trap photons

inside of a reflective volume until the photon reaches an SiPM. These designs are exciting but less mature in their research and development.

Total detection efficiency and effective areas are useful quantities to compare the performance of various optical detector designs. The total detection efficiency is the product of the probability for a photon to reach a photon detector, the probability of a photon which reaches a detector to reach a SiPM, and the quantum efficiency of the SiPM to convert the photon signal to a charge signal that can be read out by electronics. Effective areas are similar. They are defined as the cross sectional area of the detector facing the drift volume multiplied by the probability of a photon which reaches a detector to reach a SiPM, and the quantum efficiency of the SiPM to convert the photon signal to a charge signal that can be read out by electronics. Both of these quantities will be referenced throughout section 3.3.

3.3 The ProtoDUNE Designs

There are three designs which are being built as part of the protoDUNE detector. They are the double-shifted light guide, the dip-coated light guide, and the ARAPUCA designs. [25]

3.3.1 Double-Shifted Light Guide

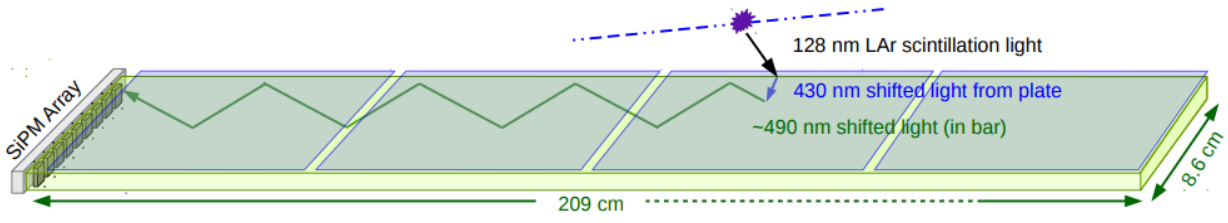

FIGURE 3.2: A diagram of the double shifted light guide concept

The double-shifted light guide design uses four groups of three passively ganged SensL SiPMs coupled to a light guide. The light guide is large, 8.6 cm by 210 cm, and intended to increase the surface area in which it is possible to detect light. The 8.6 cm by 210 cm size, along with the space for the SiPM circuit boards fits into the 10 photon detector slots per APA in protoDUNE.

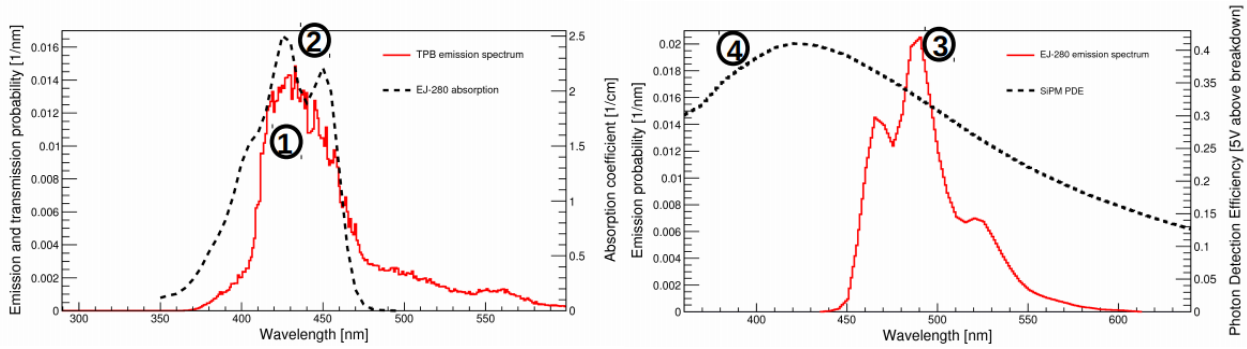

(A) The TPB emission and EJ-280 absorption spectra match up nicely. [26]

(B) The emission specturm of EJ-280 is well within the SiPM detection range. [27]

FIGURE 3.3: TPB, EJ-280, and SiPM emission, absorption and PDE specturms.

This increased surface area increases the uniformity of the detector response. There are two disadvantages of conventional light guides. First, they rely totally on internal reflection to transport photons from one part of the bar towards the SiPMs. Second, the wavelength shifting coating necessary to make incident light detectable by the SiPMs often reduces the attenuation length of light through the guide. The double shifted design addresses these shortcomings by first shifting the wavelength of light on radiator plates outside of the guides themselves. And second by using a light guide made of scintillating plastic. It is actually the TPB-doped radiator plates which shifts the light. These plates are effective in converting the emitted vacuum ultraviolet (VUV) light to 430 nm blue light. The scintillating light guide is a fluorescent plastic called EL-280 manufactured by Eljen Technologies. Its peak absorption is in the 430 nm range while its emission is around 490 nm green light. While the SensL SiPMs used in the Double-Shifted Light guide designs are slightly less efficient at detecting this 490 nm light compared to 430 nm light, this wavelength is still well within the effective operating range of the sensors.

Light measurements of double-shifted light guides suggest that their overall detection efficiency inside of DUNE of about 0.23% per detector module. This corresponds to an effective area of 4.1 cm^2 per detector module [2]. These values correspond to the designs deployed in protoDUNE. By adding double ended readouts and adding reflective material as well as other potential improvements, it is expected that these values may be improved over two fold by the time updated photosensors are deployed in the DUNE Single Phase 10kt Far Detector.

3.3.2 Dip-Coated Light Guide

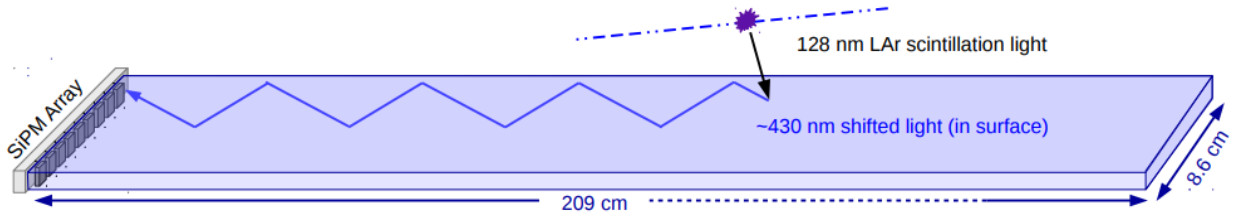

FIGURE 3.4: Diagram of the dipcoated light guide concept

In some sense the Dip-Coated Light Guides have the most straight forward design of all of the candidate light collection systems. A TPB-based wavelength shifting coating is applied in a controlled mechanical process. Light incident on the TBP coating will be shifted to 430 nm and transported within the bar via total internal reflection. If this 430 nm light reaches one of the 12 channels of SenSL Series C SiPMs, it will reach it at the SiPM's peak detection spectrum. The few pieces of the design and the controlled process of the coating application give it potential for a high degree of scalability and uniformity of response.

Light measurements of dip-coated light guides suggest that their overall detection efficiency and effective area are comparable to the double-shifted design of about 0.23% and $4cm^2$ respectively. These values correspond to the designs deployed in ProtoDUNE. By adding double ended readouts and adding reflective material as well as other potential improvements, it is expected that these values may be improved over two fold by the time updated photosensors are deployed in the DUNE Single Phase 10kt Far Detector.

3.3.3 ARAPUCA

The word arapuca refers to a bird trap used by indigenous groups in Brazil and Argentina. The ARAPUCA design for the PDS of ProtoDUNE exploits what is called a dichroic filter. A dichroic filter is a material that allows transmittance of light below a cutoff wavelength, but is reflective to light above it. In this way photons can be wavelength-shifted behind the dichroic filter and thus trapped in a small space covered with reflective coating and photosensors.

(A) An arapuca trap used for catching unsuspecting birds.[28]

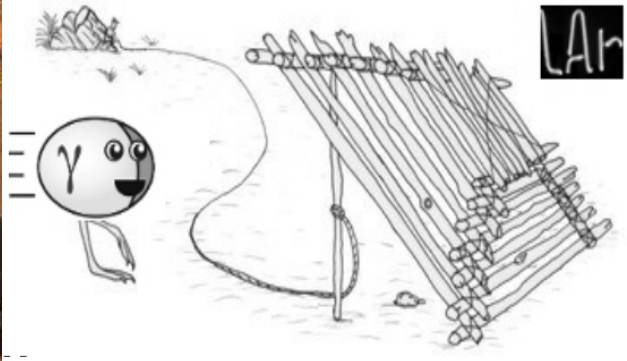

(B) Arapuca traps in ProtoDUNE are used for catching unsuspecting photons. [27]

FIGURE 3.5: These images illustrate two types of arapuca traps being used.

ARAPUCA designs are less mature than the previous two designs which have had extensive R&D, however they are quite promising systems. ARAPUCA refers not to a specific design but to a set of design schemes being developed as part of ProtoDUNE and also other LArTPC experiments. The designs in ProtoDUNE utilize SiPMs that the manufacturer (Hamamatsu) designed and marketed specifically for use at cryogenic temperatures. This decision was informed by experience using other SiPMs which were not intended for cryogenic temperatures and which performed inconsistently. These SiPMs are all ganged together passively.

A dichroic filter is transparent to light below a cutoff wavelength. However, above the cutoff wavelength the material is reflective. On either side of the dichroic filter are wavelength shifters that ensure the dichroic filter has optimal results. The first wavelength shifter is called p-Therphenyl which shifts incident 128 nm light to a range in which the dichroic filter has well-characterized behavior, around 350 nm. In most designs there are actually two dichroic filters, one with a cutoff of 400 nm and one with a cutoff of 460 nm for reflected light which may have a larger wavelength. The second wavelength shifter converts the 350 nm light to 430 nm light which is reflective to the dichroic filter and which had a high photon detection efficiency (PDE) within the Hamamatsu cryoMPPC SiPMs. Once the light has passed the layers of wavelength shifters and dichroic filters it will enter a volume that is surrounded by reflective material and SiPMs. The

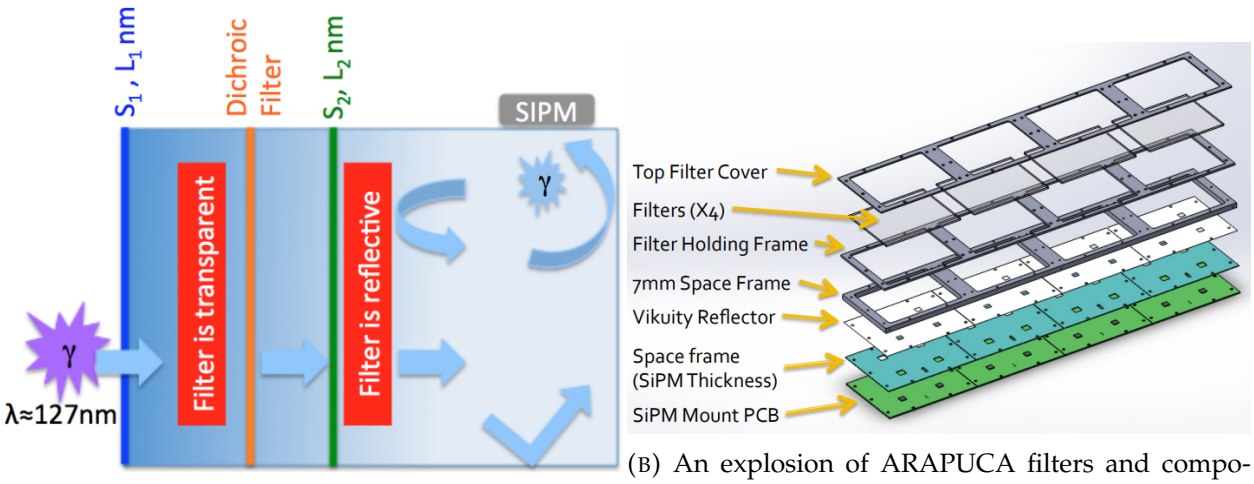

(A) Cartoon explaining the basic mechanism of ARAPUCA light traps. [27]

(B) An explosion of ARAPUCA filters and components [27]

FIGURE 3.6: Two schematics illustrating the principle of light trapping within ARAPUCAs utilizing dichroic filters as well as their design.

light may be reflected dozens of times before reaching an SiPM and still be detected.

Most ARAPUCA detectors are 7.8 cm by 9.8 cm. Therefore they are much smaller than the other two designs being considered. For protoDUNE, four of these detectors are mounted into an arm of similar size to the double-shifted and dip-coated light guides so that they may be installed in the same same slots on the APAs. These holders of groups of four ARAPUCA detectors are called cartuchos. There are many possibilities for the ganging of SiPMs within ARAPUCA systems. There is exciting ongoing research in the feasibility of ganging ever more SiPMs even across multiple individual detectors. Alternatively, the increased segmentation of the smaller detectors could be extremely useful in some reconstruction tasks, for example in reconstructing supernova events as will be discussed in the in chapter 5.

Different geometries and filter configurations have been tested for various ARAPUCA designs. Different overall detection inefficiencies for different ARAPUCA schemes have been measured at about $.4 - 1.8\%$ total detection efficiency corresponding with different effective areas which vary from 5 - 23 cm^2 [2]. All of these values are per cartucho.

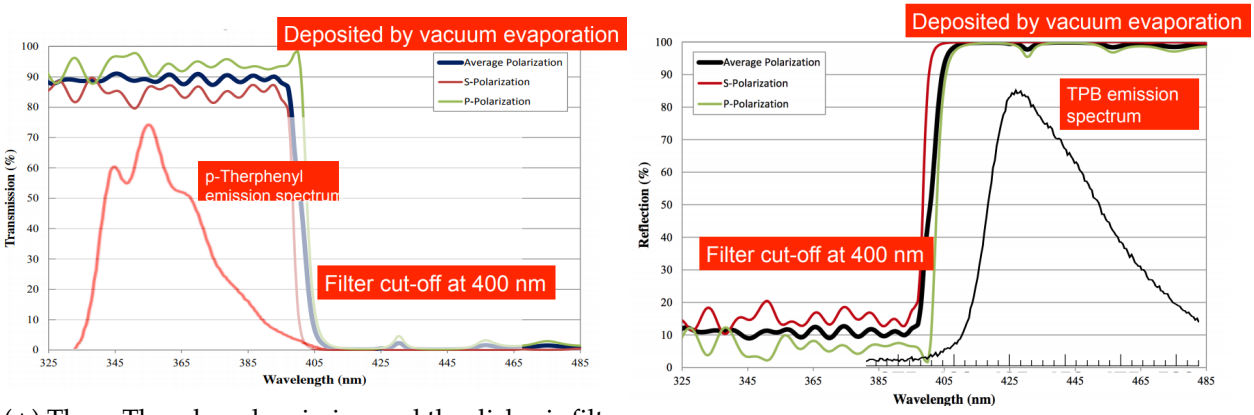

(A) The p-Therphenyl emission and the dichroic filter response spectra.

(B) The TPB emission and dichroic filter response spectra.

FIGURE 3.7: The combination of dichroic filter and wavelenght-shifting layers of the ARAPUCA are designed to shift light such that it easily passes into the detector and shift it again so that it can hardly escape. [27]

3.4 Potential Improvements for DUNE Designs

There are several proposals which may significantly improve the light detection efficiencies and scalability of any potential design. One popular idea is to introduce more SiPMs to the light guides. This could be of the form of double ended readouts or even adding more SIPMs along the edges of the detector or simply adding more within ARAPUCA cartuchos. Adding more and more SIPMs is challenging because it becomes expensive not only to purchase more devices but also to add more and more readout channels. There are additional considerations about heat dissipation and the concern that adding more penetrations into the cryostat could create opportunities for contamination to enter the liquid. Contamination such as water, oxygen, or nitrogen can greatly reduce the attenuation length of light within the detector. It is therefore with great potential importance that NICADD continues to explore the feasibility of ganging more SiPMs together on single channels. Early results look promising.

Entirely new designs are still possible, although time is beginning to run short. There are suggestions of combining the phospherescent capabilities used in the double-shift light guides with the trapping capabilities of the ARAPUCA devices to create an even more efficient photon detection system dubbed the XARAPUCAs. This research and development for this design is still

in its early stages.

Besides changing the design of the lightguides themselves, there are ways to improve the light yield of the volume. One idea is to coat the back side of the CPAs with a reflector which will reflect the light back towards the APA. Generally this reflector will also wavelength shift the light to the visible regime where the dispersion effects of the liquid nitrogen and the attenuation effects of the trace impurities will be less significant. While the dispersion and attenuation effects of the 128 nm light is generally manageable for light from within the 3.6 m drift volume, the reflective backs will greatly the distance some of the light will need to travel to the APA. There are also suggestions that the space in between the light guide modules be angled and coated with reflectors [2].

Chapter 4

PRODUCTION AND TESTING OF SILICON PHOTOMULTIPLIERS

4.1 Silicon Photomultipliers

Silicon photomultipliers (SiPMs) are pixel arrays of pn diodes. When operated under sufficient reverse bias, they are capable of detecting faint light signals. If reverse biased above a critical voltage, known as the breakdown voltage, the field within the depletion region of the diode is strong enough that a single charge carrier within the region will have sufficient energy to excite and release electron-hole pairs as it is accelerated to the anode or cathode. These secondary carriers will each create additional electron-hole pairs and so on until there is an avalanche of charge flowing in the direction of bias. This run away behavior is remarkably easy to control with a simple resistor in series with the device. As the current increases due to the cascade, the voltage drop across the resistor increases until the voltage drop across the pn junction is less than the breakdown voltage. Once below this voltage, the avalanche will be quenched. In this way, the absorption of a single photon can be amplified to an easily measurable and recordable discrete electric signal. If a SiPM is reverse biased past this point of breakdown, it is said to be operating in Geiger mode. [29]

SiPMs are generally attractive to particle physicists because they are relatively unaffected by the electric and magnetic fields present, are compact, and cheap compared to traditional photomultiplier tubes. In the context of the DUNE and ProtoDUNE detectors, their uniformity of performance and cheapness are attractive.

The primary challenges of using SiPMs as the basis of a photon detection system in a LArTPC

are that they must be robust enough to survive the temperature of liquid Argon of around 87 K. Working with the SiPM manufacturers, especially those who are active in developing next generation cryogenic SiPMs may be the best way to address this challenge [30]. The devices must also be able to detect the characteristic 128 nm vuv scintillation light of liquid argon. Most conventional SiPMs have detection efficiencies which peak at 400 - 500 nm. Several strategies for shifting the wavelength of incident photons were discussed in the chapter 3. Additionally, some manufacturers are intentionally designing SiPMs sensitive to this VUV light [31]. Furthermore, the DUNE far detector is quite large, whereas the SiPMs offer little coverage. SiPM coverage can be increased by ganging the SiPMs together. Again, certain manufacturers are leading the way in designing products that can meet this need [32]. These new technologies are exiting, but untested. Ganging of large numbers of SiPMs, while feasible, presents its own challenges. Both the testing of the cutting-edge photosensor products as well as testing the limits of ganging are the subject of ongoing research and development efforts in NICADD.

4.1.1 Gain

The gain of a detector refers to the size of the output signal for an individual photons. It is therefore a vital measure of detector performance.

The gain can also be calculated by

$$G = \frac{C\Delta V}{q} \tag{4.1}$$

[29] Where C is the capacitance of pn junction, ΔV is the voltage above the breakdown voltage and q is the fundamental electric charge. Clearly gain is related to the size of the pixels (via the capacitance) and the amount of overvoltage.

One way to measure the gain of a SiPM is to put the SiPMs in an environment with no light. Signals will be produced due to thermal noise or to cosmic ray interactions. After recording a sufficient number of pulses a histogram can be made where pulses are binned according to the size of their adc signals. An example of this is shown in figure 4.1. The different, evenly-spaced peaks in the figure correspond to different numbers of photoelectrons. The distance between consecutive peaks is the gain.

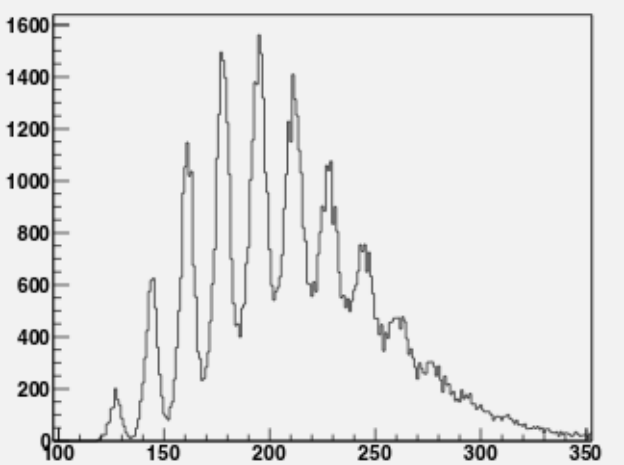

FIGURE 4.1: This plot shows how the gain per PE can be measured. The y axis is the number of events per adc bin. The x axis is adc. By examining a histogram of all adc counts of all waveforms distinct peaks are obvious. These peaks come at regular adc intervals because they correspond to signals originating from an integer number of PE. The gain corresponds to the number of adc between each peak. [33]

4.1.2 Breakdown Voltage

The operation of a SiPM exploits the change in behavior of charge carriers at the breakdown voltage of the pn junction. In order to effectively operate these sensors, it is necessary to supply a voltage 2-3 V above the SiPMs breakdown voltage. SiPMs purchased from the manufacturer will never have exactly the same breakdown voltage but will have some distribution. In the double-shifted and dip-coated photon detection systems of ProtoDUNE three SensL SiPMs will be ganged together. In order to ensure that the output of these detectors is what we expect, we must ensure that these three sensors have breakdown voltages relatively close to the same value. It is even more critical to characterize the breakdown voltages of individual devices for the ARAPUCA systems in ProtoDUNE because some ARAPUCA configurations have 12 sensors ganged together. Furthermore, an active and relevant area of research and development for more efficient are ways to gang a larger number of SiPMs together.

The breakdown voltage can be measured via two methods. The first is by the equation above:

$$G = \frac{C\Delta V}{q} \tag{4.2}$$

We can take data for events with variable voltage above the overvoltage (where we get a response). Because there is a linear relationship between G and ΔV, we can plot G vs ΔV, and meaningfully fit a line to it. The point on the V axis where the line intersects is the breakdown voltage.

There is also a faster and more convenient way to measure the breakdown voltage. If we measure the current across the the SiPM while while incrementing its reverse bias, we measure an iv curve like the one shown in figure 4.2. Clearly at low reverse bias (below the breakdown voltage), the sensor behaves like a normal diode in that it does not allow current to pass. Above the breakdown voltage the current increases rapidly due to thermal excitations of electrons.

To define a breakdown "point" we notice that the slope is greatest near the breakdown point we wish to define and decreases for high ΔV. By plotting the inverse slope of this graph, and fitting a line to the points above the breakdown voltage, the point where the line intersects the V axis is a reasonable measure of the breakdown voltage.

It is possible to measure the breakdown voltage in about a minute using the ivscan method whereas the gain method requires several data runs of a few minutes a piece. For the production testing of thousands of Protodune sensors the ivscan method was therefore selected.

4.1.3 Noise

As we've mentioned before, thermal excitations are always present. In fact, the current in the ivscans above are all derived mostly from individual thermal electrons hole pairs causing cascades. If there is too much noise it can mask the interesting photon signal. Optimal performance requires a low noise rate. Because the probability for thermal excitations is directly related to temperature, so the current, noise, and effective breakdown voltage are all dependent on temperature. It is not surprising that the noise rate at room temperature (20 C or 293K) is much higher than the noise rate at cryogenic temperatures (-186 C or 87 K). "Normal" rates for 6x6 mm SensL C series at room temperature tend to be around 2000 kHz, while at cryogenic temperatures are closer to just 20 Hz.

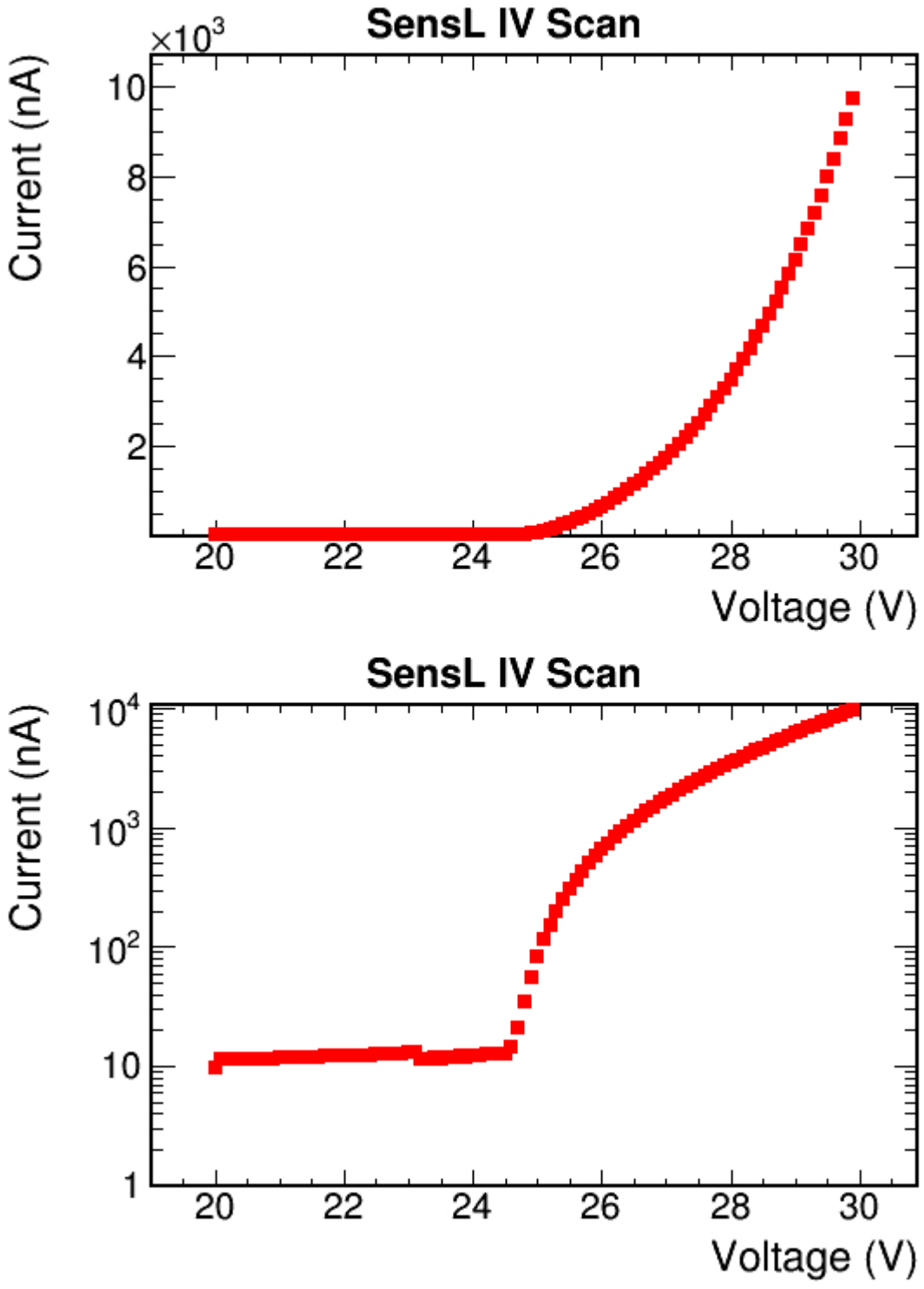

FIGURE 4.2: An ivscan of a group of SensL C series SiPMs

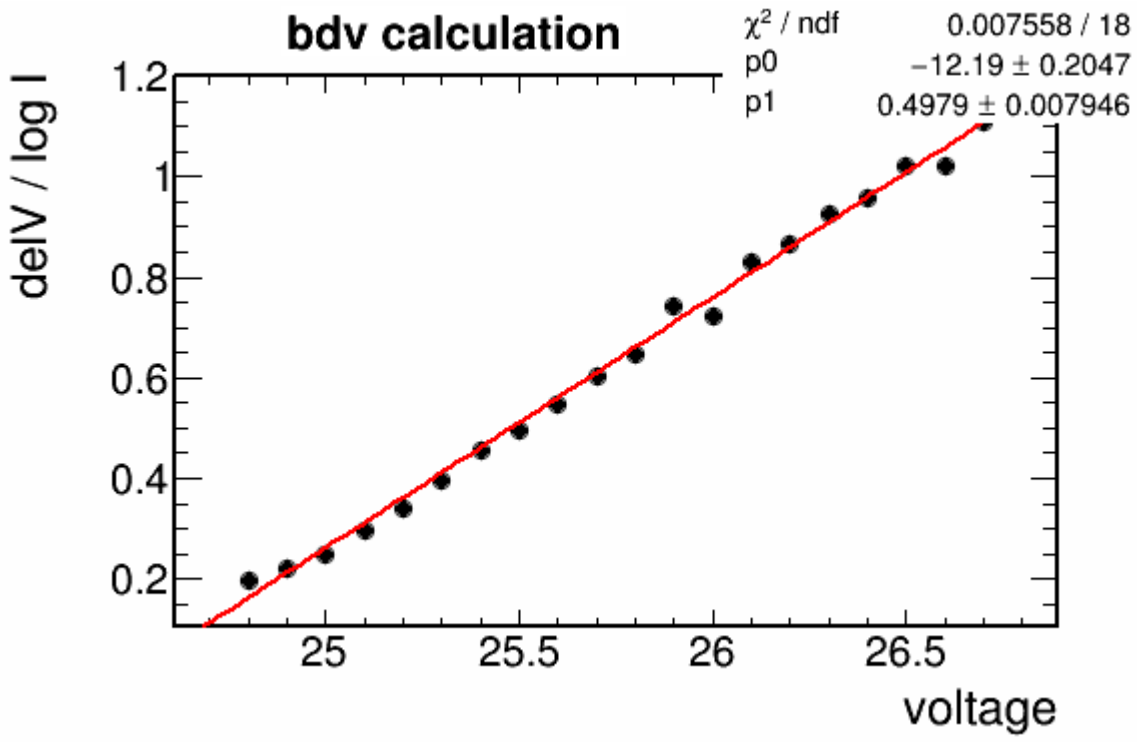

FIGURE 4.3: A plot of the inverse slope of the log of current from an iv scan vs voltage

4.1.4 Crosstalk

The process that produces a signal in an SiPM is a group of charged particles being accelerated by an electric field. Because accelerated charged particles produce light, it is possible for an avalanche in one pixel may cause an excitation in an adjacent pixel. In this way, what ought to have been recorded as a single PE may be recorded as a multiple PE signal. This is called the crosstalk and is present in any silicon pixel detector. One way to quantify how much this is happening in the detector is to look at the rate of two PE signals and divide it by the rate of single PE signals while the detector is reverse biased in a totally dark environment. The chance for coincident thermal excitations simultaneously is relatively low, so this is a reasonable measure of how much of the cross talk effect is present in the device.

4.2 Production testing of SensL SiPMs

6mm by 6mm SensL SiPMs were used for the majority of photon collection systems in Proto-DUNE. They have a spectral range which peaks around 420 nm that the dipcoated and double wavelength shifting lightguides were designed to utilize. They are relatively large by SiPM standards with pixel sizes of 35 μm by 35 μm, making them efficient detectors. [34]

4.2.1 Warm Tests

These detectors were ordered from SensL and stored in a vacuum oven to limit exposure to humidity. Protection from humidity is critically important in the time just before they are soldered onto their circuit boards. Warm tests were performed on the sensors en masse using a 3D printed plastic container called a "waffle pack" coupled to a "pogo board". The pogo board has 16 pairs of spring loaded connectors soldered to a circuit board which could be plugged into a voltage control and readout system the FEB, or front end board. The pogoboard was mounted on the FEB inside of a dark box so that the sensors would be exposed to no ambient light during testing. With the pogo board we could test large quantities of detectors relatively quickly with no soldering. The plastic container containing up to 16 sensors was coupled to the pogo board using either screws located

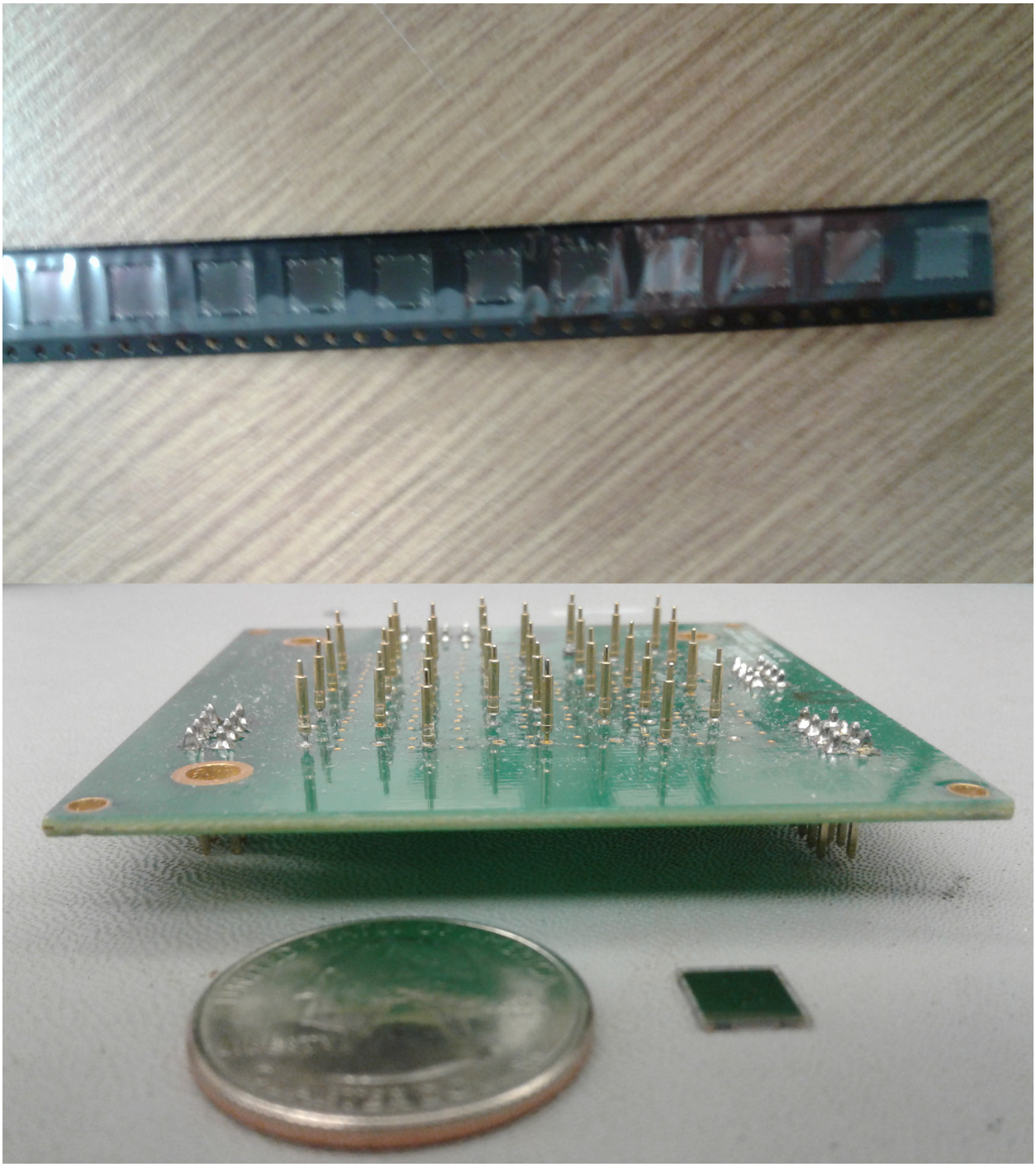

FIGURE 4.4: TOP: Image of a row of SensL SiPMs in the manufacturer's packaging tape. BOTTOM: The pogo board, an individual SensL SiPM, and a quarter for scale.

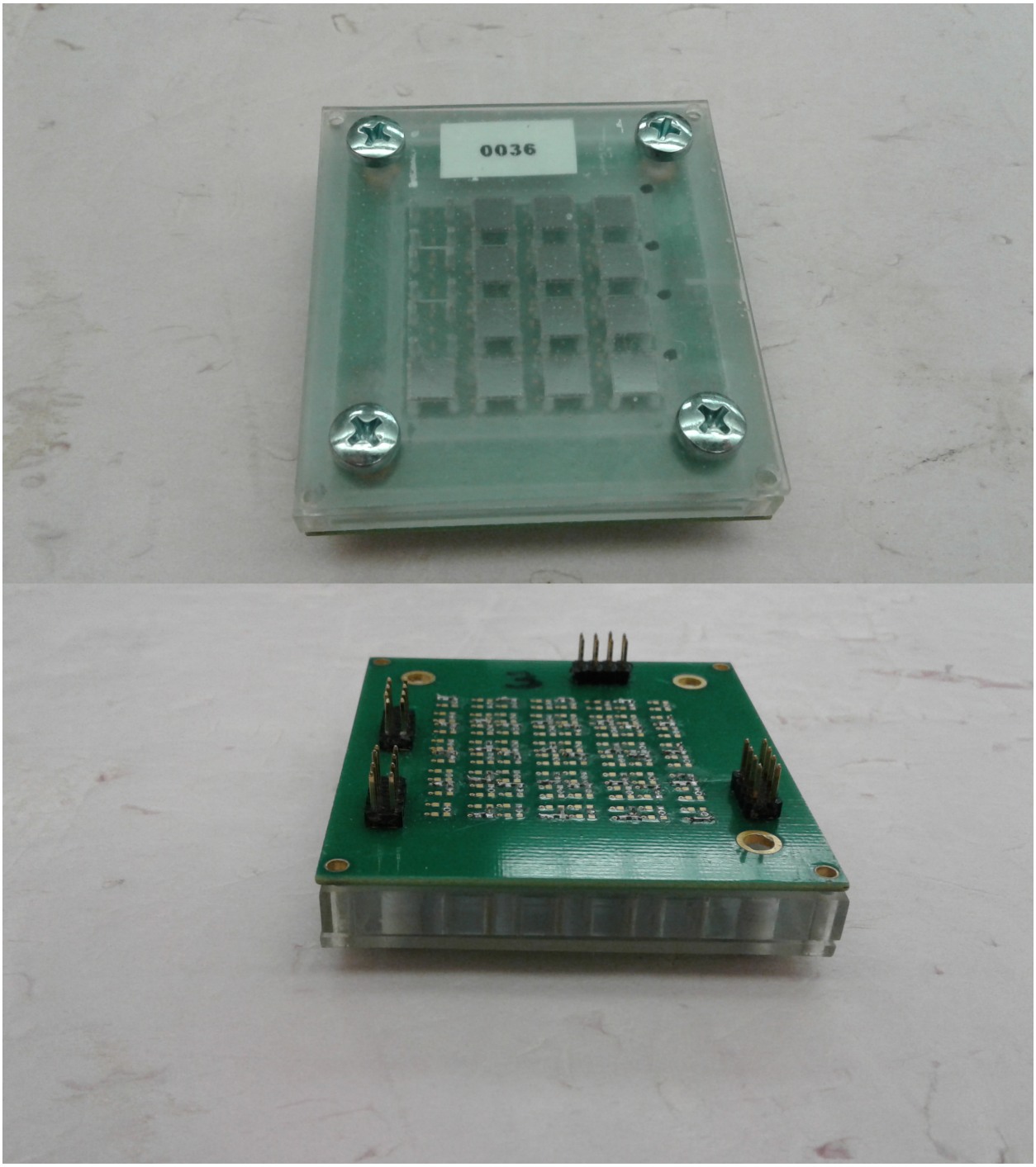

FIGURE 4.5: TOP: Top view of a pack attached to the pogoboard BOTTOM: Bottom view of a pack attached to the pogoboard.

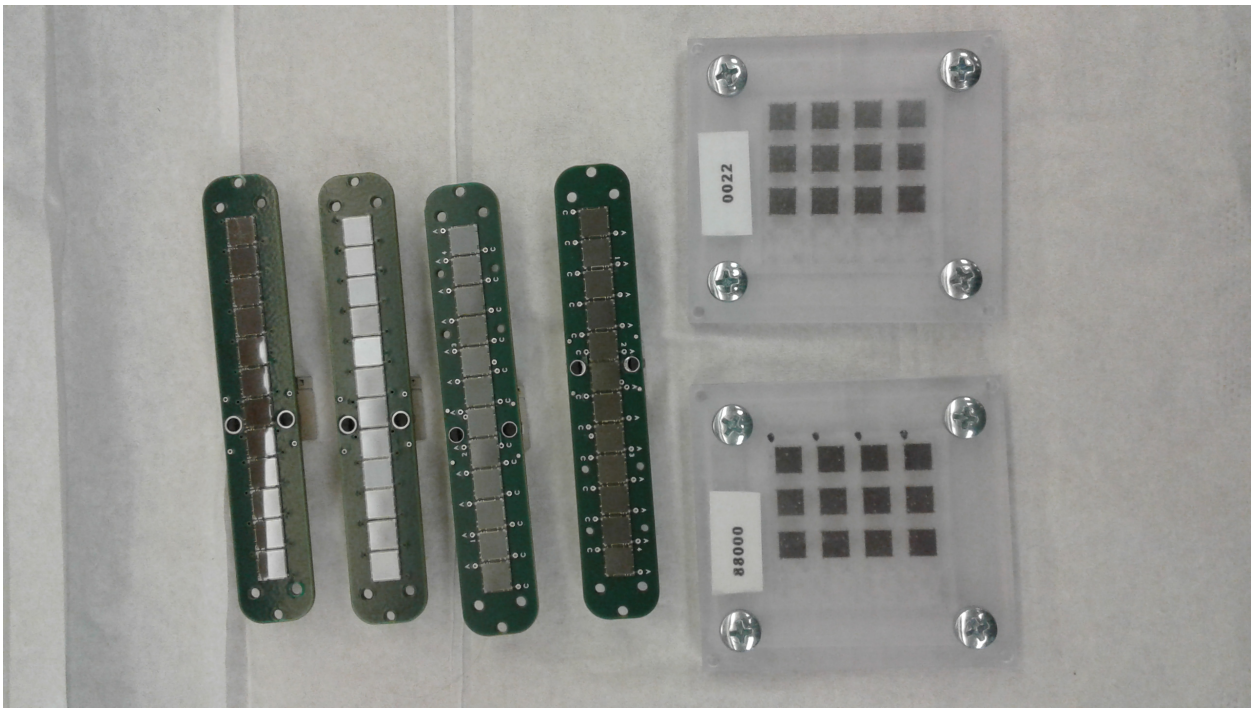

FIGURE 4.6: Fully assembled circuit boards with SiPMs, also called hover boards, and waffle packs shown together.

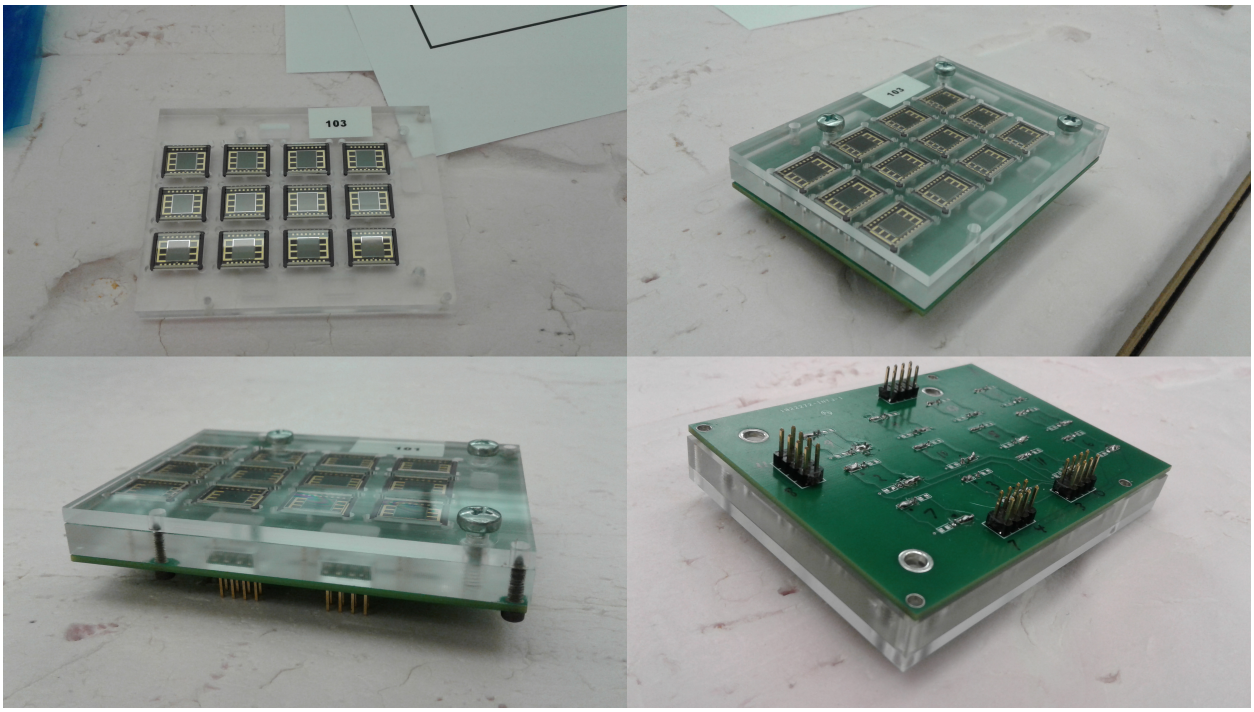

FIGURE 4.7: TOPRIGHT: Top view of a pack filled with cryoMPPCs destined for an ARAPUCA sensor TOPLEFT: Top view of the pack with cover, mounted on a pogo board BOTTOMLEFT: Botom view of the pack with cover mounted on a pogo board BOTTOMRIGHT: Angled view of the pack, with cover mounted on the pogoboard and fixed with the screws.

in the corners of the container and circuit board or with elastic devices. Once the entire system was plugged into the FEB, software could automatically take ivscans of each individual sensor. Analysis of the IV scans gave measurements of current at 24 V (about 0.5 V below the breakdown voltage) and 28 V (about 3.5 V above the average breakdown voltage). Additionally the individual breakdown voltages would be measured. After the iv analysis, a data run was performed in total darkness, and with a controlled flashing of an LED with 12 ns flashes. Analysis of the dark runs yielded gain and noise values for the sensors. The led run was an additional test of the gain and ensured that the sensors respond properly to light. A final analysis script checked to ensure that all sensors were within an acceptable limits of noise, gain, breakdown voltage and current at both 24V and 28V. Those outside of the acceptable ranges were rejected. Packs of 12 SiPMs were sent via overnight delivery to Colorado State University to limit their exposure to humidity before soldering. Colorado State quickly soldered in groups of 12 onto the circuit boards. The time the SiPMs spend outside of the vacuum oven until the time they were soldered was never to exceed three days.

4.3 Cold Tests

The strategy and procedure of cold testing went through iterations during the production testing of the ProtoDUNE SiPMs. Initially individual SiPMs were not cold tested whereas circuit boards mounted with SiPMs underwent cold tests in liquid nitrogen at both NIU and CSU. This was a reasonable strategy for the first few hundred devices. SensL, the manufacturer of SiPMs used in ProtoDUNE, changed their production methods once or multiple times for later batches. While the minor changes to the production methods produced SiPMs which were still within the specifications SensL advertised, they were no longer reliable for the cryogenic temperatures needed for ProtoDUNE. SensL was informed, but had no interest in returning to the old methods. When it was realized that certain batches of sensors were unable to survive one or more dippings in liquid nitrogen, cold tests were no longer performed on the circuit boards. The final batches of SiPMs were so unreliable that a decision was made to dip the devices in liquid nitrogen before warm tests so that those SensL devices which immediately cracked could be thrown away.

FIGURE 4.8: An image of the cold test stand the cold test stand.

4.4 Cold Tests of Circuit Boards

In the center of figure 4.8 is the liquid nitrogen dewar. In this picture it had been sitting in an open configuration on a humid summer day which is why it is covered in ice. Above the dewar is a plastic lid which may be closed. This lid has a flexible, foamy attachment on the bottom which can form a pseudo seal on the dewar. It is held in place by tightening the screws attached to the two guide rods on either side of the dewar. Not visible in this picture is a small hose attached inside the lid which leads to a tank of dry nitrogen gas. This gas can flow into the lid to displace the ambient air and significantly reduce the humidity on the inside. Also attached to the lid is a temperature and humidity sensor which is used to monitor the conditions under the lid. Above the dewar is a holder which can hold up to three cables. Attached to these cables are the "hover boards" which are the circuit boards containing the twelve sensors which ultimately will be coupled to the double-shifted or dip-coated light guides. This holder is also attached to an arm and motor controller which can raise and lower the hover boards at a controlled speed. When voltage is applied to the sensors the entire system can be shut inside of a light tight box which can be seen around the entire stand.

For the cold testing done in the context of ProtoDUNE we attached one hover board to the connector cable. The cable was connected to the readout hardware designed for ProtoDUNE and intended for use in DUNE. This custom hardware is produced by the collaboration and called the SiPM Signal Processor (SSP). Using the SSP it is possible to set adc thresholds for events and to view their wave forms. The SSP also sets bias voltages and reads out data. The SSPs have gone through multiple iterations over 2016-2018. To simulate as best as possible the conditions of ProtoDUNE, the exact cable specifications were used. This is a 30 ft teflon coated cable capable of reaching all of the sensors in the full ProtoDUNE configuration. There were significant challenges when this cable picked up sporadic radiofrequencies, perhaps due to NICADD's location across the street from the DeKalb Police Station. These signals could be suppressed by looping the cable through a magnetic core. It also seemed that orienting the plane of the loop parallel to the direction of the police station suppressed these signals. This cable orientation is shown in figure

4.9. Additional spurious signals frustrated measurements that were related to unstable cable connections. These issues could be largely resolved by ensuring there was no tension at any of the connector locations (due to changes in SSP design there were necessarily cable adapters which introduced extra connection points). These issues which plagued measurements in the beginning were addressed throughout the summer of 2017.

FIGURE 4.9: An image of the SSP cable configuration. The 30 foot cable is looped through two magnetic cores and oriented to reduce its ability to act as a radio antenna.

Testing would begin by pouring liquid nitrogen into the dewar and turning on the SSP. A hover board would be attached to the end of the cable when the motor controller was in its uppermost position. After the bottom of the lid formed a seal with the dewar, the hover board would then be lowered into the dewar lid. Once inside, dry nitrogen gas would flow at around 30 psi. At least 20 - 30 minutes were allowed to allow the dewar to equilibriate and the SSP to "warm-up." During this time the humidity inside of the lid was monitored. In the winter the relative humidity within the lid could drop below 1 %, while in the summer it would be a struggle to get below 5 %, sometimes requiring increasing the pressure of the nitrogen gas. Once the humidity was

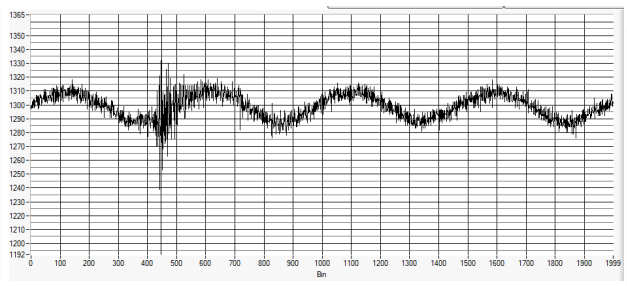

(A) Radiofrequency ringing possibly from nearby police station. These signals can be suppressed by looping cable through magnetic core.

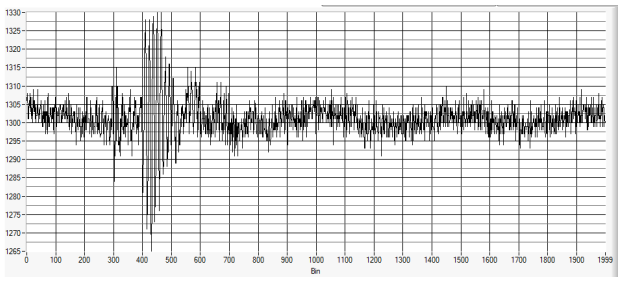

(B) Large quickly oscillating signals appear when one of the connections on the cable is under stress.

FIGURE 4.10: The two screenshots above illustrate the early problems encountered when using the SSP.

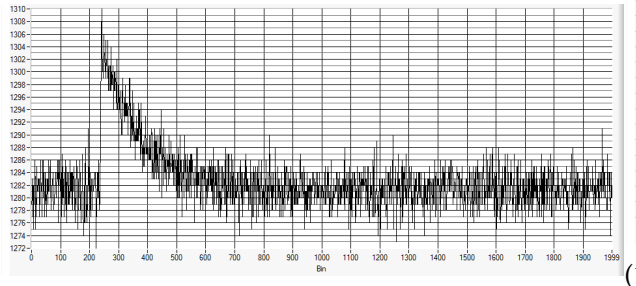

(A) A beautiful, clear photon hit recorded on the SSP.

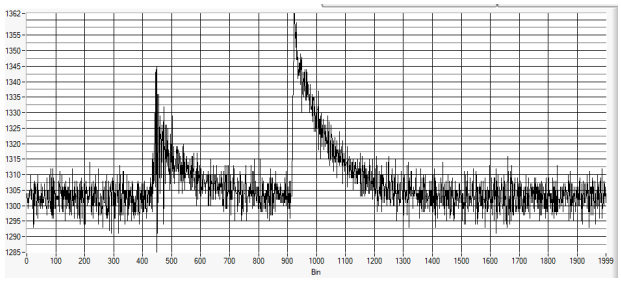

(B) A screenshot of the SSP recording two photon events with different PE within the same event window.

FIGURE 4.11: The two screenshots above illustrate the types of signals the SSP is intended to measure.

determined to be as low as possible, the motor controller would be set to begin dipping the board at 1 cm per minute.

The first primary danger of cold testing is temperature shock. This is particularly true during the insertion of the hover board into the liquid nitrogen. The second primary danger of cold testing is humidity. This is particularly dangerous when extracting the hover board. Once out of the liquid nitrogen it will be by far the coldest thing in the environment and regardless of how low the humidity is, there will always be at least a little water condensation on the surface of the circuit board.

The see-through lid allows the scientist to visually observe the board as it enters and exits the liquid. It is also important to audibly observe the board during the insertion. Because liquid nitrogen is so much colder than room temperature, there is always some boil off. This boiling becomes audible when the board is being dipped too fast. It is always heard once the metal connector of the hover board, which is attached to a warm 30 m cable, enters the liquid. Best practice is to listen for the boil as it is dipped and to pause the motor when it is heard. Generally this means that there will be several pauses, particulary when the connector reaches the liquid. Another effect which can sometimes audibly be heard is the sound of a SiPM cracking due to the extreme low temperatures. This virtually always happens during the insertion of the board. Most of the time it happens to one of the sensors near the connector during the time that the connector reaches the liquid. Though the caution and slowness described in this paragraph mitigates how much stress these SiPMs are under, these SensL SiPMs are really not designed, manufactured, or warrantied for these sorts of environments. Indeed the lowest recommended operating temperature of these devices as listed on the SensL data sheet is -40 C [34]. This is over 150 degrees hotter than liquid nitrogen. The caution required in dipping these devices means that the lowering process takes around 40 minutes.

Once the devices are submerged in liquid nitrogen, the system needs 20-30 minutes to equilibriate. Otherwise the temperature of the cable would still be changing, affecting any measurements.

Once the dipping procedure is completed, the SSP is used to set biases well below the breakdown voltage of the detectors. At these temperatures the breakdown voltage is several volts lower

than it is at room temperature. Generally biases were set at 15 volts. Each of the four channels was set to take pulse data with this bias. Any pulses measured in this configuration are thermal noise in the electronics. Doing these runs gives the pedestal or the lowest possible adc setting we can trigger on without picking up useless noise. The first measurements we take are meant to define what threshold we should use as a trigger later on. They were runs of 10000 "triggered events," triggered with a negligible threshold.

Once these trigger thresholds are determined for each channel, we took runs of 200,000 events at the determined threshold with the bias set to 25.5 V (approximately 2.5 V above breakdown voltage). These triggered runs are relativity quick to take and are meant to confirm that gain and rate measurements are reasonable. Once we've confirmed that everything looks reasonable and that there are no connection issues, we take random data. The random data is the most unbiased and reliable data to characterize the performance of the SiPMs. 800,000 random events are taken at 25, 25.5, 26, and 28 volts for each of the four channels on the board.

After all of the data are taken, the voltages on the SiPMs are set to zero. Then the dark box is opened and the motor controller is turned on. By now the dry nitrogen gas has been flowing in the lid for a few hours already, but the humidity should be checked to ensure it was at a low level. The motor controller would be set to a higher speed of about a cm every few seconds. Once the hover board was above the dewar and totally within the acryllic lid enclosure, a separator could be inserted between it and the dewar. This would allow the hover board to warm at a reasonable rate. Once the temperature inside of the lid reached about 12.5 C the gas would be turned off. One it reached about 18 C the board was considered warm enough to reintroduce into the ambient environment. The hover boards were stored in an oven set to 40 C to help limit the humidity they would be exposed to during storage as well as to dry out any residual moisture from the extraction.

4.5 Cold Tests of Individual SiPMs

As discussed earlier, later batches of SiPM devices would physically crack when subjected to cryogenic temperatures. This problem was so severe that we began dipping SiPMs before any warm

tests so that devices that were doomed to fail would not be mounted onto a circuit board and damage an entire channel of a light detector. The initial dipping procedure is nearly identical to that of circuit boards. Instead of attaching a circuit board to a cable, SiPMs still in the packaging tape were put into a bag attached to the motor arm with a zip tie. The bag was lowered in the same slow, humidity-controlled way as described in section 4.4. The amount of failures varied greatly between batches, between about 0 - 30% failure rate. The sensors were left submerged for about a half hour and then raised following a similar procedure to that described at the end of section 4.4.

Chapter 5

SUPERNOVA SIMULATIONS AND FLASHMATCHING

5.1 Motivation

Timing information is not an obstacle for measurements involving interactions of beam neutrinos in the DUNE Far Detector. This is because beam spills are generated with precise timing. In the case of proton decay events or supernova interactions, there is no such luxury. These interactions may occur at any time. Knowing the time of interaction is critical to understanding an event if it is recorded. The time that the TPC system records an event could be delayed by 0 to around 2.4ms depending on how far away from the TPC the ionization electrons are required to drift. Another result of the LArTPC utilizing an exceptionally large drift volume is there are significant variations in the shape and size of pulses recorded by the TPC which also depend on how far away an event was from the APA plane. To accurately reconstruct the energy of any interaction it is imperative to know the position in this x direction. Because of the single plane geometry of the APA and the fine 4.75mm spacing of the wire channels, it is very good at measuring the y and z coordinates of an event, but reconstructing x positions is more challenging. Therefore in studies of events that are not generated with beam timing information, the utilization of the photon detection system becomes especially important. The time between the recorded light collection (which for the purposes of theses studies corresponds exactly to the initial time of the event itself) and the recorded charge collection (which is driven by the strength of the electric field and how long it takes electrons to move towards the drift plane which is $\mathcal{O}(ms)$) is measured. By measuring this

time difference, it is possible to accurately measure the x position within the detector. Knowing x allows us to make the appropriate drift corrections to measured signals.

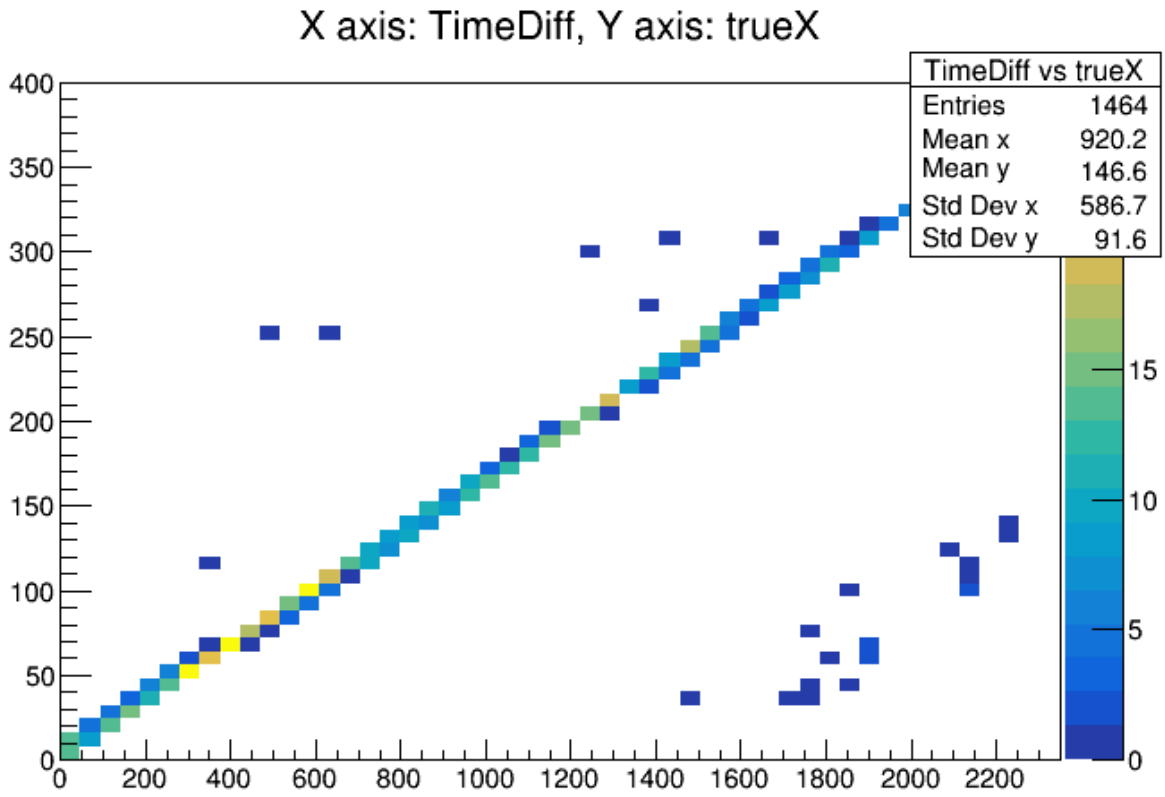

FIGURE 5.1: Time difference between photon and charge signals after full simulation and reconstruction plotted against truth x position. Because electrons are drifted through the volume at a constant velocity of $0.15 cm/\mu s$, this time difference is an excellent way to measure x position. This plot is very nearly perfectly linear with a slope of $6.7 \mu s/cm$.

5.2 Radiological Backgrounds

Finding accurate timing information is complicated by the fact that there are many radiological background signals generating photons throughout the detector volume all of the time. These background signals tend to be of low energy. This means that they can be easily suppressed in the higher energy case of proton decay events for example. However when supernova signals have sufficiently low energy, these radiologicals are a significant problem. This is particularly

true because a supernova interaction far away from the APA may look a lot like a lower energy background closer to the APA. Furthermore the rates of radiological signals are high enough that there can be flashes caused by multiple decays which pile up on the detectors to appear like a single, higher energy flash. The most important background is the ^{39}Ar β decay. It is probably unsurprising that this decay

$$^{39}Ar \rightarrow ^{39}K^{*} + e + \overline{\nu_e} \tag{5.1}$$

can look a lot like

$$^{40}Ar + \nu_e \rightarrow ^{40}K^{*} + e \tag{5.2}$$

Other important backgrounds that have even closer energies to the supernova signal are the beta decays of ^{85}Kr and ^{222}Rd.

5.3 Simulations and Reconstruction

Most DUNE supernova studies use a software called MARLEY [35] [36] (Model of Argon Reaction Low-Energy Yields) to generate supernova events. It takes our best estimates of supernova neutrino spectrum and calculates the outputs of electron neutrino and argon charged-current reactions. The way it performs these calculations is outside the scope of this paper but is guided by both theoretical calculations, previous measurements of supernova neutrinos in the 1987 event [37] [38], and well established nuclear models. The outputs of these reactions are inputted into LarSoft simulation software and labeled as corresponding the truth supernova interactions. The results of MARLEY simulations are saved in a special type of file that LArSoft reads known as artroot files. These files may be used as inputs to a Geant4 simulation.

The Geant4 simulation within LArSoft is set up to look only at massive particles. The behavior of photons in the detector is considered separately as will be explained later. LArSoft has geometries related to the current DUNE design, and if these simulated particles deposit energy into a detector, this data is saved into another artroot file. This file can then be used as an input to

a simulation of the TPC response, converting analog signals into discrete TPC hits. The output of this simulation is the simulated raw data which again is saved in the format of an artroot file. These final products can be analyzed using either standard LArSoft tools or custom reconstruction software to to produce objects like tracks and showers.

The simulation chain for photons generally proceeds in a different, more computationally efficient, chain. For a given energy of interaction, a characteristic number of photons is produced isotropically. The position within the detector has a specific fractional visibility basically independent of the type of interaction that produced the photons. A large sample of photons has been simulated at many points within the detector to analyze the fraction that reach photon detectors. This fraction is then saved within what is called the photon library. Having a photon library greatly reduces simulation time and resource requirements. Rather than simulating tens of thousands of individual gammas for all points along all tracks in every event, it is essentially a matter of looking up a fraction from the photon library to determine how many photons actually reach the detectors. Once this is known, a simulated SSP signal is produced as simulated raw data. This signal is converted into discrete detector hits which can be used to reconstruct an optical flash event.

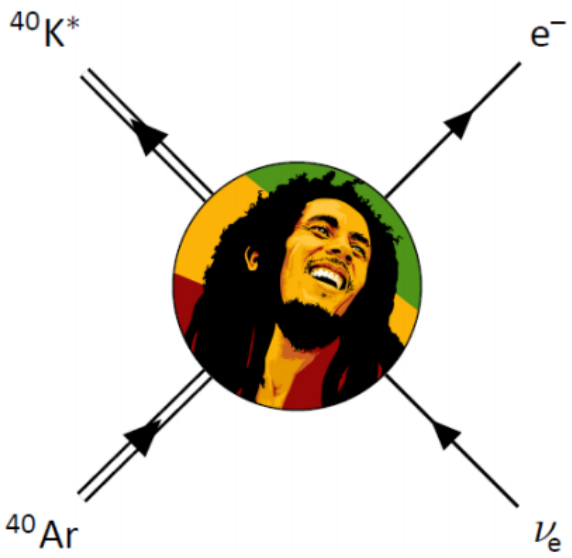

FIGURE 5.2: The official logo of MARLEY software. The official goal: To determine "whether everything gonna be alright" for SN physics in LArTPCs. [35] [36]

The sample used in this analysis is MARLEY supernova interactions simulated along with radiological interactions. The computing group at DUNE has performed the full reconstruction chain for these events and there are currently 990 datasets of 100 time windows containing one MARLEY supernova event and backgrounds. To speed up the production and analysis, only a section of the detector is simulated in the dataset. Most DUNE simulations only use the section of detector called the 1x2x6. This is 1 APA wide (though there are really two drift volumes back to back), 2 APAs high (y direction), and 6 APAs long (z direction).

5.4 Flash Matching

The results of the simulation and reconstruction described in the previous section are saved in artroot files. A flashmatching analysis configuration file is used to extract the important information from each of these files. Significantly it can extract truth information about the supernova event. It also extracts every reconstructed flash with information like when it occurred, where in the yz plane it occurred, how many PE were in the flash. For each event there are typically dozens or hundreds radiological flashes and only one or zero supernova flashes. The goal of the flash matching study is to select from these flashes one which is the best candidate to be a supernova event and to check how often we are right (by cheating and looking at the truth information).

The most useful input to perform this flashmatching is the total PE of each of the flashes. The total PE is arguably most important as the energy spectrum of supernova neutrinos is larger than the radiological signals. It is significantly larger than the endpoint energy of the Ar39 beta decays. A first order attempt to find supernova flashes simply by looping though all of the flashes in an event and selecting the larges one is surprisingly effective.

Another useful input is truth position in the yz plane. The TPC itself is pretty good at distinguishing between supernova and background events and can reconstruct an event vertex on the yz plane with an accuracy of a few cm. Therefore the yz position of the supernova signal is something that we expect to have when we are really taking data. By knowing this position, we can ignore all reconstructed flashes whose positions are sufficiently far away. Unfortunately because the current design of the PDS involve photon detectors spaced 2.4 m apart, the position resolution

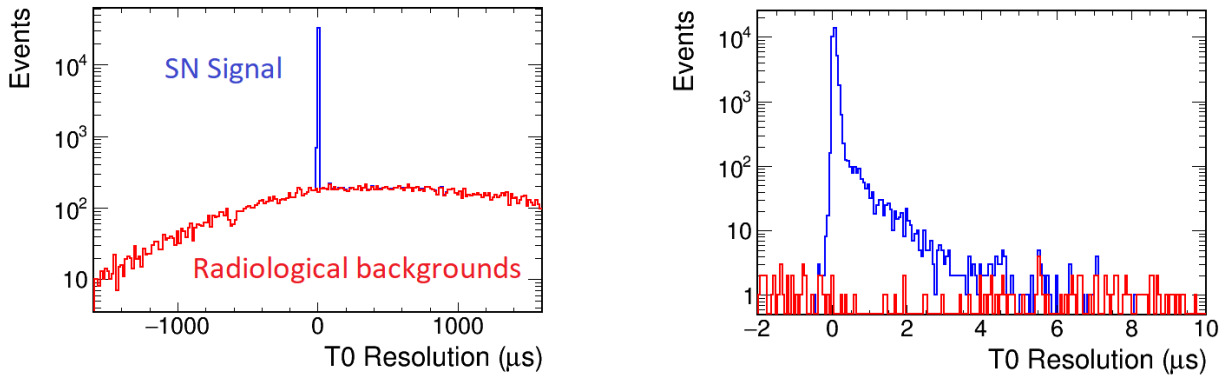

FIGURE 5.3: This plot shows the selected flash time minus truth time. The blue plot represents selected flashes which where reconstructed out of photons from the simulated supernova interaction signal. In other words, the blue plot represents flashes chosen correctly. The red plot represents flashes reconstructed out of photons originating entirely from radiological backgrounds. In other words the red line corresponds to flashes chosen incorrectly. The plot on the right is the same plot zoomed in. The width of the blue spike is less than 100 ns. There is also a tail which corresponds to the late light that extends a few μs. This plot shows that when a flash is chosen correctly, precise timing information is given to an interaction. The plot assumes a detection efficiency of 4.1 cm^2, corresponding to a double-shifted light guide design like the ones deployed in ProtoDUNE.

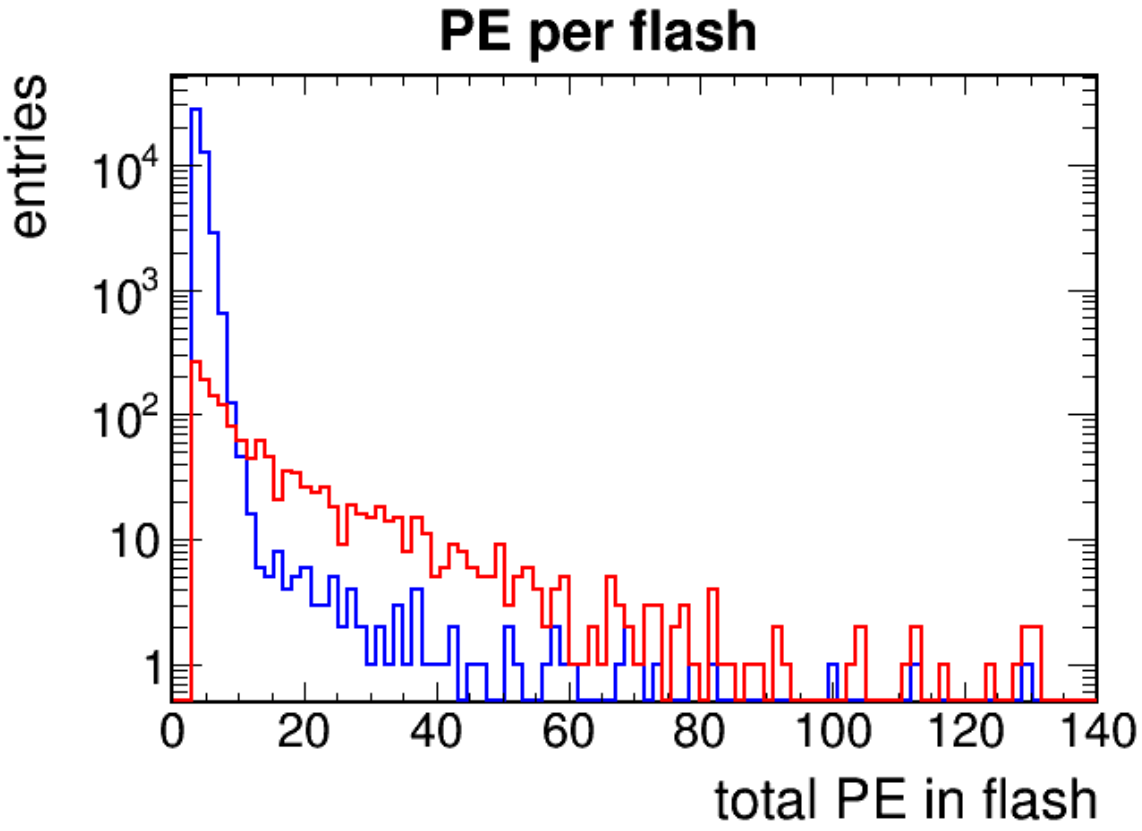

FIGURE 5.4: The PE per flash for truth supernova flashes (shown in red) tends to be larger than the PE per flash of the radiological signals (shown in blue). However there is clearly significant overlap

of the reconstructed flashes is not very good. This inaccuracy drives the optimization of how far away from the truth event position we look. For example if we look at only flashes which are several cm of the truth event position, we are ignoring many events which could have occurred in the correct position, but whose flash was reconstructed in another position. Furthermore if we allow ourselves to look in too wide of an area, there is a greater possibility that there will be a radiological event very close to one of the photon detectors which will produce an anomalously large PE signal. The optimal radius from the truth yz position to look is around 240 cm. Using this information you can loop through all of the flashes in an event, select only those within 240 cm of the truth position on the yz plane, and then select the largest PE signal within this subset of flashes. Adding this single distance cut significantly improves flashmatching capabilities.

5.5 Flash Matching Efficiency

Now that we have a simple algorithm for selecting flashes, it may be useful to see how well it performs not only overall, but also depending on what the energy of the supernova interaction was. Unsurprisingly, the algorithm performs better for the higher energy interactions, as illustrated in figure 5.9a. Likewise, the selection process works best when the interaction is near the collection plane as shown in figure 5.9b. This is because farther away from the interaction the light will become more disperse and attenuated.

We can now define a flash matching efficiency. The definition is simply the number of flashes which are chosen correctly over the total number of supernova flashes. Example plots of the efficiencies for flash matching are shown versus x and E in 5.9. In chapter 3 we discussed several photon detector designs under consideration for the DUNE Far Detector. It would be interesting to directly compare how different designs compare in their ability reconstruct and match flashes. It is not obvious how much of a benefit a more effective detector is. On the one hand if it sees more light, it has a better chance of producing signals which can be more easily separated from backgrounds. On the other hand the number of background flashes and the total number of PE within those flashes will increase with increasing light collection abilities.

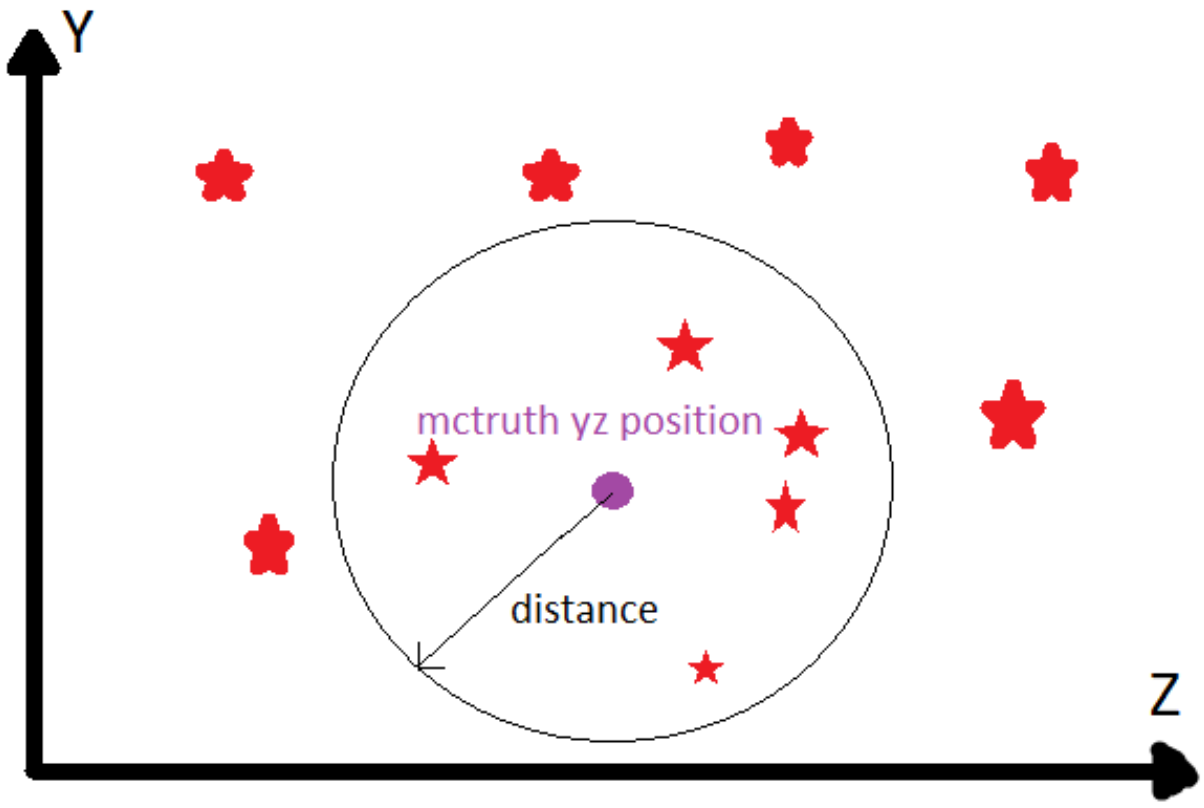

FIGURE 5.5: This cartoon illustrates how the distance cut works. For a given event there are hundreds of flashes all over the *yz* plane. Because we know from truth or TPC information the location of the supernova event of interest on the *yz* plane, we can consider only those flashes within a given distance

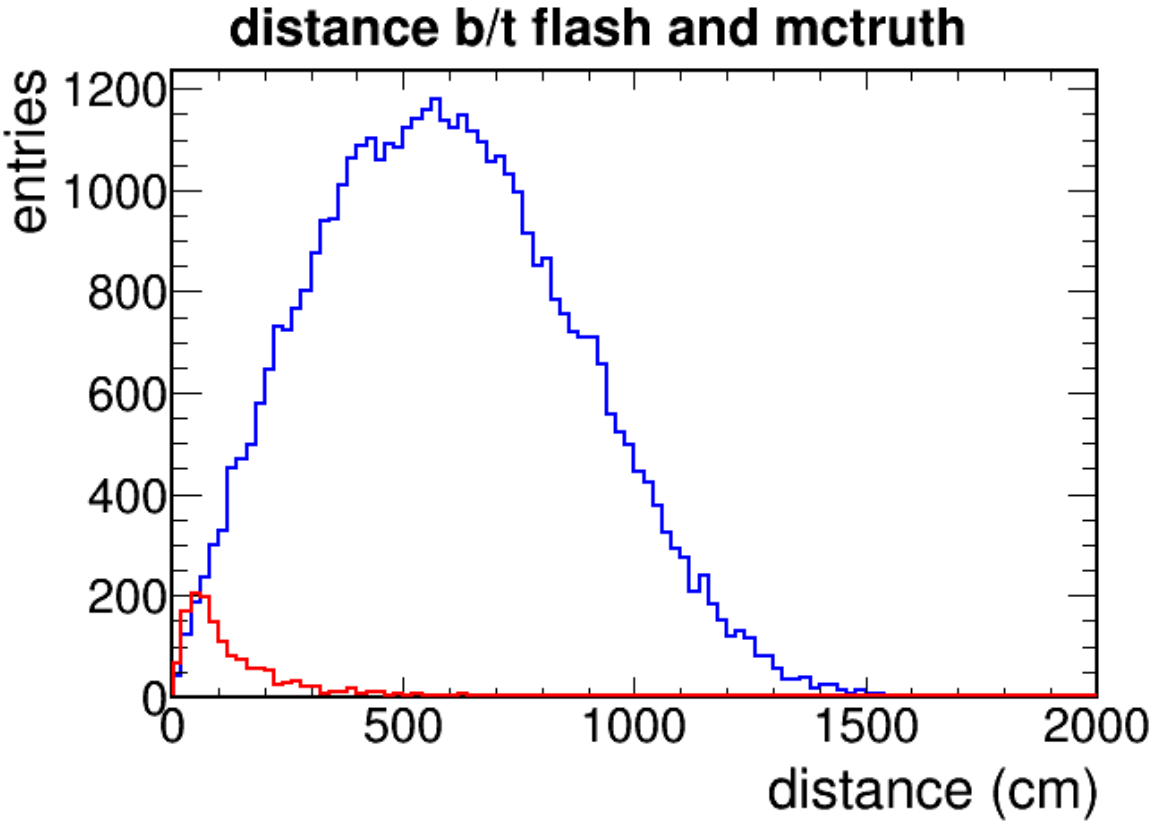

FIGURE 5.6: The distance from the truth supernova event *yz* position is unsurprisingling less for supernova flashes than for the average radiological flashes. However because there are radiological flashes everywhere, there is still significant overlap. The peak of the distance for supernova is driven by the position resolution of the photon detection system. The peak of the distance for radiological flashes is driven by the geometry of the 1x2x6 detector slice we use in this simulation.

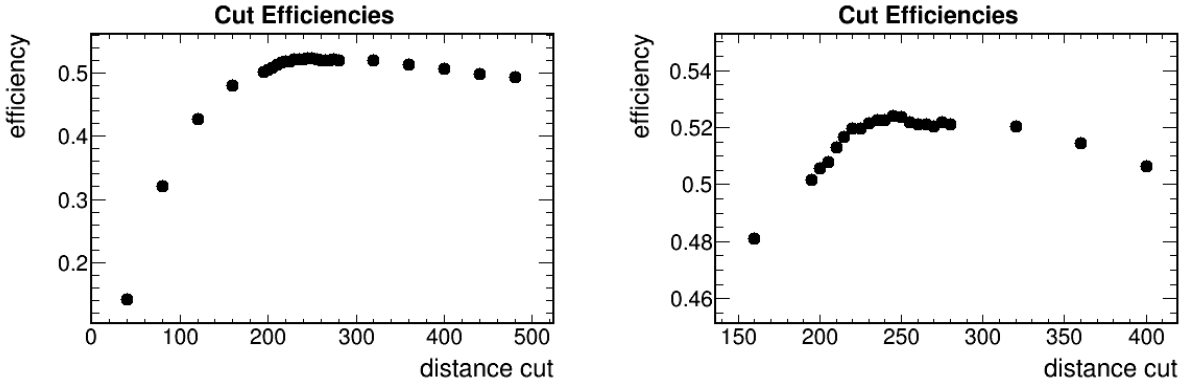

(A) (B)

FIGURE 5.7: Above shows the efficiency of selecting the supernova flash versus the length of the distance cut.

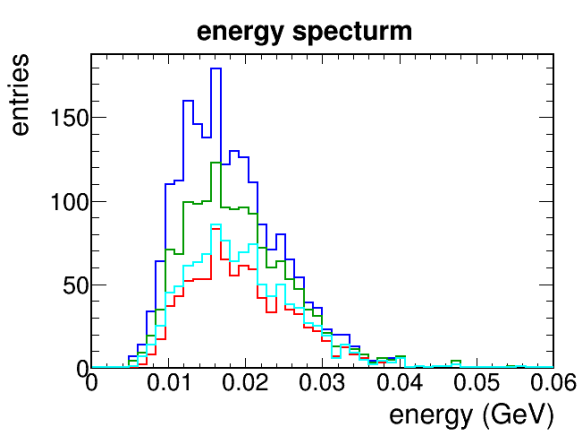

(A) The energy spectra

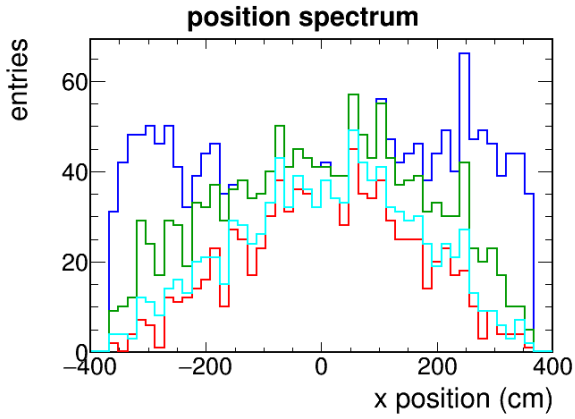

(B) The position spectra. X=0 corresponds to the APA plane.

FIGURE 5.8: The blue line shows the truth spectrum for the 2000 events in this sample. The green line is the spectrum for supernova events that have a flash which is reconstructed. Red is the spectrum of supernova flashes we are able to choose correctly simply by selecting the largest flash in the event. Cyan is the spectrum of supernova flashes we choose correctly by choosing the the largest flash within 240 cm of the truth position on the yz plane.

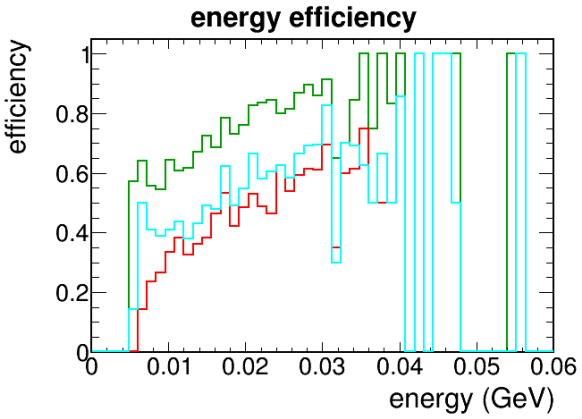

(A) The energy efficiencies spectrum.

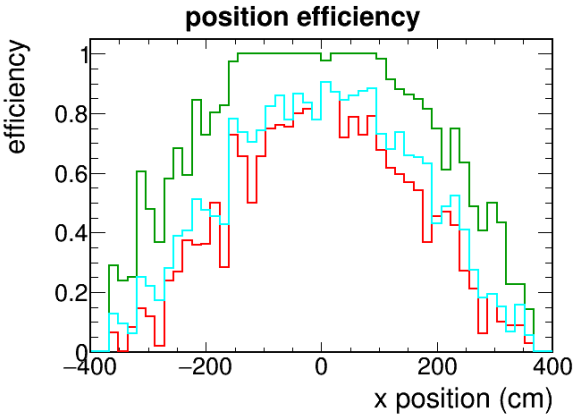

(B) The position efficiency spectrum

FIGURE 5.9: The green line is the efficiency spectrum for supernova events that have a flash which is reconstructed. Red is the efficiency spectrum of supernova flashes we are able to choose correctly simply by selecting the largest flash in the event. Cyan is the efficiency spectrum of supernova flashes we choose correctly by choosing the the largest flash within 240 cm of the truth position on the yz plane.

To compare different designs directly, we can use the value called the effective area as the basis for comparison. The effective area was defined previously in chapter 3. It is the total area of the light detector multiplied by the average probability for a photon incident on the detector to be converted to an electrical signal. In the section 5.3 we described the simulation of the photons within LArSoft. Essentially photons are simulated isotropically at many points throughout the detector volume and the number that ultimately reach detector determines the "visibility" of a given point. This collection of visibilities is stored in the photon library. The visibility for a given location can be looked up during a simulation so that tens of thousands of individual photons do not need to be simulated every time LArSoft is run. This creates a problem because assumptions about the detector geometry and efficiency are built into the library. This is especially significant for the ARAPUCA designs because they have a very different geometry compared to the other light guide designs. The standard version of LArSoft simulates light using geometries, quantum efficiencies, and attenuations which correspond to the double-shifted design.

For this analysis we do an end run around most of the problem by exploiting the definition of effective areas. In LArSoft the parameter that controls the efficiency of the detector is called the quantum efficiency, QE. Also in LArSoft the attenuation of light as it is propagated through the light guide is implemented in a c++ file which can be looked up. The average attenuation, $\bar{A}$ can be found from integrating over the length of the guide. The geometry of the light detectors is saved in a special geometry file. Here one can find the length ℓ and height h. Effective area, EA can be defined in terms of LArSoft parameters as

$$EA = \ell \times h \times \bar{A} \times QE/0.7 \tag{5.3}$$

The factor of 0.7 is meant to account for the efficiency lost to the photon detectors due to the shadow from the charge collection wires. It is just a factor added into the simulation but needs to be corrected for if we want to think about how an EA in LArSoft compares to a measured EA of a photon detector during some test. If one were to change ℓ or h, it would require constructing an entirely new photon library for each different detector. This is very expensive in time and computation power. However we can adjust QE because it just enters the library as a scale factor.

It is currently possible to resimulate only the photon detection system response separate from the rest of the simulation and to adjust the QE by changing a single value in a configuration file. This allows us to make very good comparisons between different designs with different effective areas using existing code. It is not a perfect solution. For example some ARAPUCA designs have greater segmentation in the z direction which should lead to greater spatial resolution in the yz plane. This will not be accounted for in this study. There is a lot of active work going on within the photon simulation group and new tools are being built to address this problem. For the rest of this paper however, we will just be adjusting QE to get a desired EA.

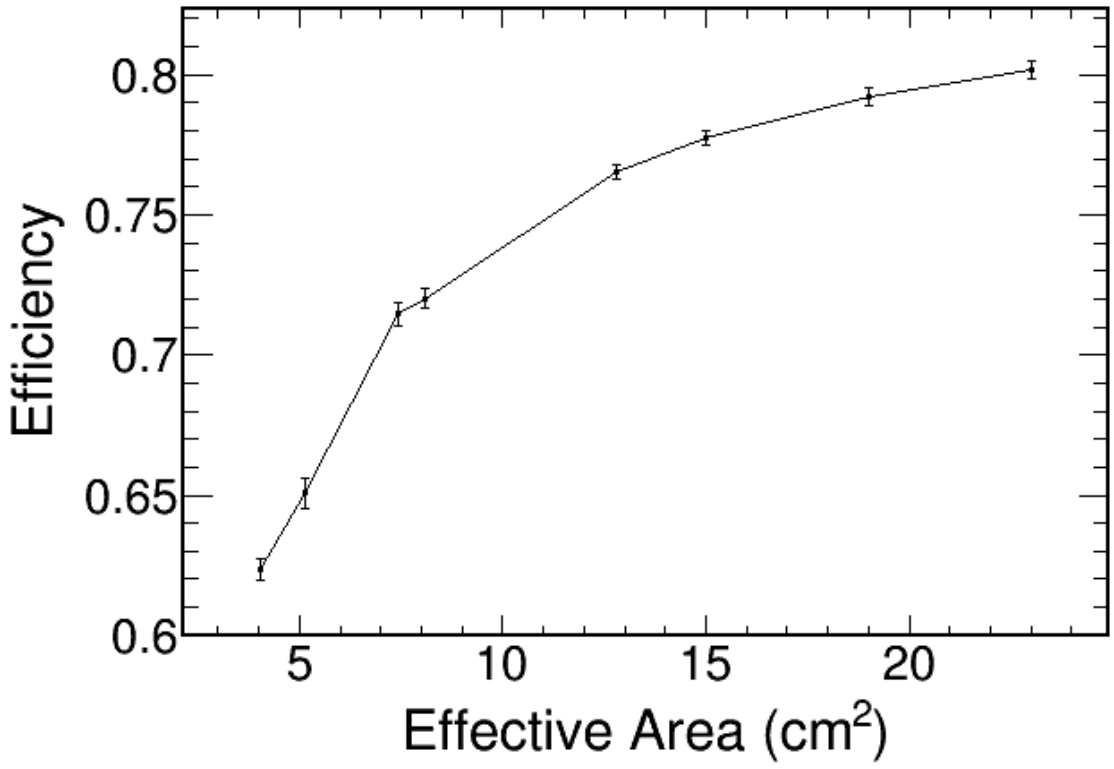

FIGURE 5.10: The flashmatching efficiency improves with greater light collection abilities. Notice that the gain is less than linear.

The average performance of different effective areas is illustrated by the plot in figure 5.10. By increasing the effective area, flash matching efficiency is improved with diminishing returns. The efficiencies in position and energy for 4, 8, and 23 cm^2 detectors is illustrated in figure 5.11. Clearly

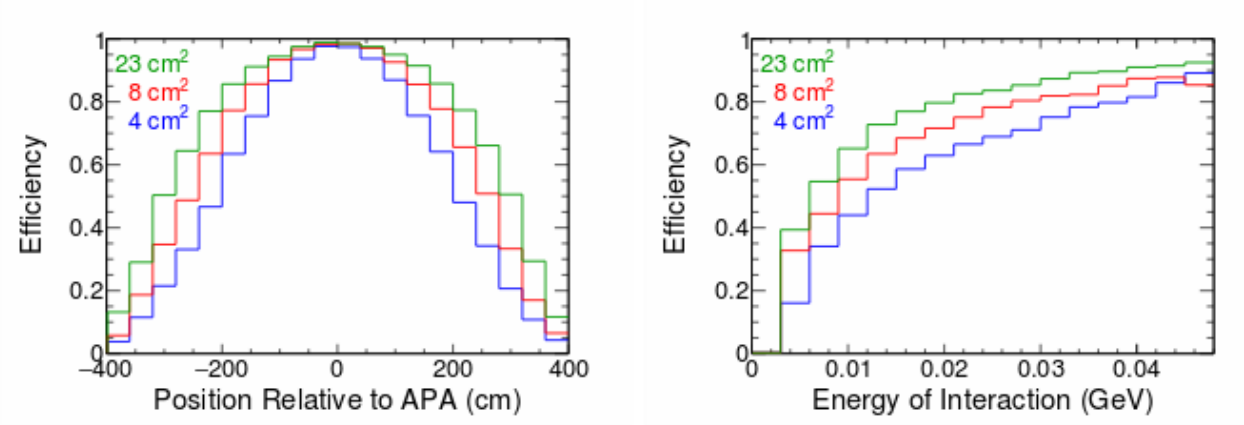

FIGURE 5.11: These figures are analogous to figure 5.9 but show three different effective areas plotted together. Unsurprisingly the lower effective area designs perform worse and the difference is most pronounced at low energies and far from the detection plane. These plots also appear in the technical proposal [2]. Blue corresponds to the effective area similar to the dip-coated or double-shifted designs. Red corresponds to the effective area of these photon detectors if a second set of 12 SiPMs were attached to the opposite end of the light guides. Green is the most optimistic of the current ARAPUCA designs.

the larger effective areas improve position uniformity and are more sensitive to lower parts of the energy spectrum.

5.6 Threshold Study

One assumption which has not been addressed is the assumption that during a supernova it will be possible to read out every flash. This may not be true. Because the flashes may occur at any time and the electronics will be sampling on the order of a few hundred ns, there will be a lot of samples per detector module per second. Because of the sheer size of the DUNE detector and the goal for DUNE to be reading out continuously for 30 seconds if it goes into supernova neutrino data taking mode, reading out all of the flashes would result in a unwieldy amount of data. This is an even larger problem for high effective area designs since they will be more sensitive to radiological flashes. This section explores the possibility of buffing data and only reading out flash information if it is above some threshold. A simple way to do this is to define some PE threshold and require that at least a single detector be above it before it is read out. In these studies the same MARLEY

+ radiological simulations are used. To calculate the rate, a time window in the event is selected so that it only includes radiological flashes. This gives a handle on how large the background data rate is for different thresholds. This data rate is then scaled by 8.3 to go from the data rate in the 1x2x6 volume to that of a full 10 kt detector module. This scaling makes the assumption that because the dominant source of backgrounds are located throughout the volume, the data rate will scale with the volume.

Efficiency against effective area and efficiency against rate plots are shown in figure 5.12. It is clear that the larger thresholds diminish both the flash matching efficiencies and the data rate.

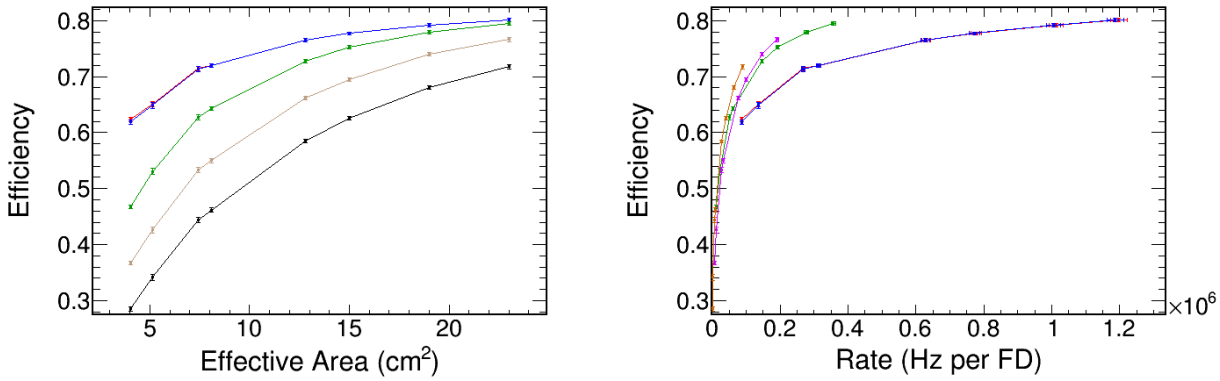

FIGURE 5.12: In these plots each point corresponds to a set effective area and a set threshold. The color of the points describes what kind of threshold was set. Red = no threshold, blue = 1.5 PE threshold, green = 2.5 PE threshold, cream = 3.5 PE threshold, black = 4.5 PE threshold. Both plots show the same data points. The one on the left is efficiency vs effective area whereas the one on the right is efficiency vs data rate.

Another way to set a threshold is to only read out flashes that have a given number of photon detectors above 1.5 PE. This was done for 2, 3, 4, and 5 detectors above 1.5 PE. There were similar results as before, the more strict the threshold, the more the flash matching efficiency and data rate are diminished. In figure 5.13 three different PDS-threshold schemes are shown to give similar flash matching efficiencies. Two are 15 cm^2 detector schemes, one with a 4.5 PE threshold applied to the detector with the largest signal, the second with a 1.5 PE threshold applied to the three detectors with the largest signals. The last is a 4 cm^2 detector scheme with no threshold applied. These have a flash matching efficiencies of 63.4%, 63.5%, and 63.3% respectively. Interestingly,

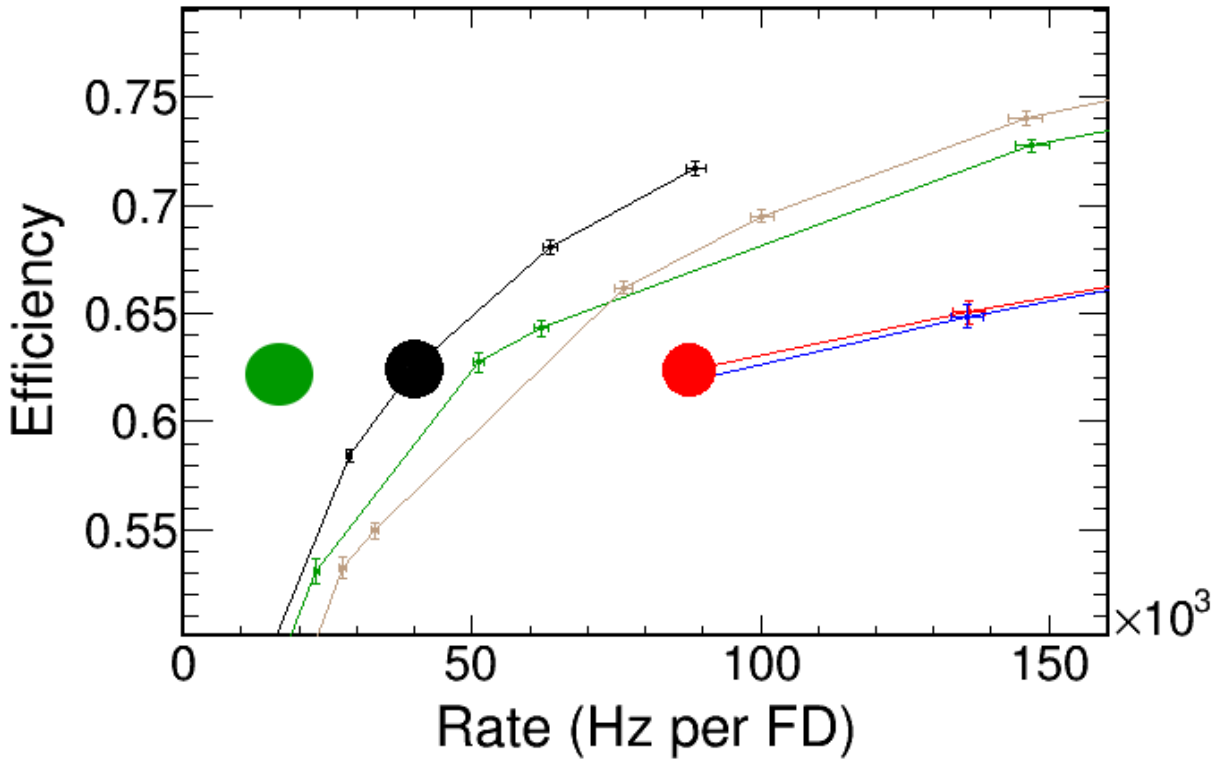

FIGURE 5.13: This is a zoomed in version of the plot shown on the right in 5.12. There is a single additional data point added which is the large green dot corresponding to a PDS of effective area 15 cm^2 with threshold requiring three detectors see greater than 1.5 PE. The large black dot is also a PDS of area 15 cm^2 but with threshold requiring one detector to have a greater than 4.5 PE signal. The large red dot corresponds to an effective area of 4 cm^2 and no threshold. All of these points have flash matching efficiencies between 62.3% and 62.5 %.

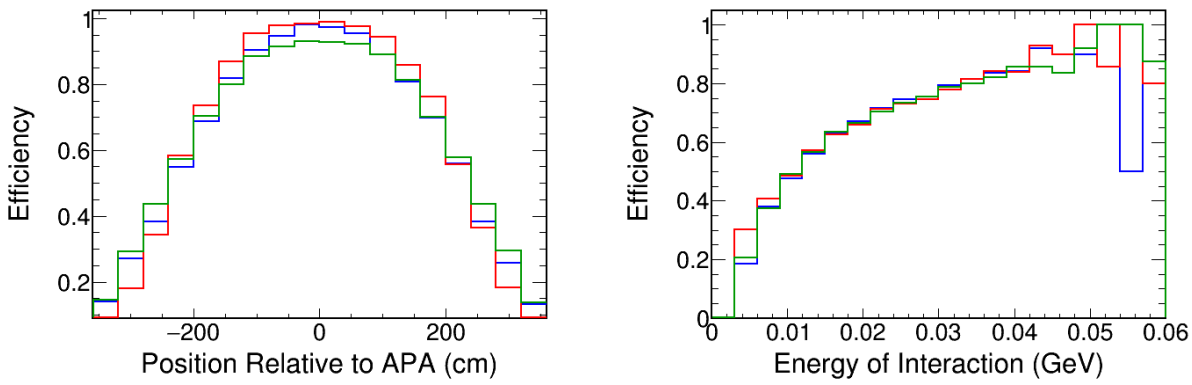

FIGURE 5.14: Even though the three schemes described in figure 5.13 have the same flash matching efficiencies, they are sensitive to a different subset of flashes. This is illustrated in the plot on the left. Requiring multiple detectors to be above a small threshold improves flashmatching for flashes far from the detection plane. The plot on the right shows that the different schemes are sensitive to a similar subset of the neutrino energy spectrum.

these three different schemes are effective at flashmatching a different subset of the flashes as shown in figure 5.14. In particular, requiring multiple detectors to be above a small threshold improves flashmatching of light signals originating far from the APA plane. By the time they reach the detector plane, the photons will have spread out. These thresholds can be improved. Already with a few simple example schemes it is clear that the data rate can be greatly reduced while maintaining a majority of the flash matching efficiency offered by a given detector scheme.

Chapter 6

CONCLUSION

LArTPCs are attractive detection systems in several active areas of physics. They integrate several detection systems, including rapidly evolving photon detection technology, to create high resolution reconstructions of particle interactions. DUNE is a large scale application of LArTPC technology whose primary objective is to make neutrino measurements of mass differences and mixing angles relevant to neutrino oscillations. The sensitivities of DUNE make it an attractive detector to study the neutrino flux of a core-collapse supernova should one occur in the Milky Way Galaxy while the far detector is operational. Measuring neutrinos from supernovae is challenging due to the combined effect of their low energy and the fact timing information must be supplied entirely by the photon detection system. Developing a DUNE photon detection system that is capable of this task will come from experience building ProtoDUNE, which will soon begin operations, as well as from simulations of supernova interactions within the detector. This thesis briefly described the physics motivation of DUNE, and gave a description of DUNE and ProtoDUNE with emphasis on the photon detection systems. Finally it discussed the tests of the SiPMs which were installed in ProtoDUNE, and the impact different photon detection designs could have in reconstructing time information of supernova neutrino interactions.

Bibliography

[1] The DUNE Collaboration *et al.*, "Dune conceptual design report volume 2: The physics program fro dune and lbnf", 2015. [Online]. Available: http://lbne2-docdb.fnal.gov/cgi-bin/RetrieveFile?docid=10688&filename=DUNE-CDR-physics-volume.pdf&version=10.

[2] M. S. Athar *et al.*, "DUNE Technical Proposal", Tech. Rep., May 2018, This is DUNE-doc-7656-v4 in DUNEdocdb.

[3] Wikimedia Commons via user MissMJ. (2007). Standard model of elementary particles. File:Standard Model of Elementary Particles.svg, [Online]. Available: https://commons.wikimedia.org/wiki/File:Standard_Model_of_Elementary_Particles.svg.

[4] G Rajasekaran, "The story of the neutrino", *arXiv*, Oct. 2016. [Online]. Available: https://arxiv.org/pdf/1606.08715.pdf.

[5] R. D. Jr., "Nobel lecture: A half-century with solar neutrinos", *Reviews of Modern Physics*, vol. 75, Jul. 2003. [Online]. Available: https://journals.aps.org/rmp/pdf/10.1103/RevModPhys.75.985.

[6] C. L Cowan Jr. *et al.*, ""detection of the free neutrino: A confirmation"", *Science*, vol. 124, no. 3212, pp. 103–104, Jul. 1956.

[7] Y. Fukuda *et al.*, "Evidence for oscillation of atmospheric neutrinos", *Physical Review Letters*, vol. 81, no. 1562, Aug. 1998.

[8] M. Thompson, *Modern Particle Physics*. Cambridge University Press, 2013.

[9] B. Wansak, *Status and prospects of juno*, Presentation at Neutrino 2018, Online; accessed 21 June 2018, 2018. [Online]. Available: https://zenodo.org/record/1286850#.Wyw0Ba0U_ak.

[10] K. Scholberg, *Neutrinos from core collapse supernovae*, Presentation for National Nuclear Physics Summer School 2013, Online; accessed 3 June 2018, 2013. [Online]. Available: http://www.int.washington.edu/NNPSS/2013/lectures/Scholberg3.pdf.

[11] J Hester and A Loll. (2005). Crab nebula, [Online]. Available: https://en.wikipedia.org/wiki/Crab_Nebula#/media/File:Crab_Nebula.jpg.

[12] G. Srinivasan, *Life and Death of the Stars*. The University of Chicago Press, 2014.

[13] Carl J. Hansen *et al.*, *Stellar Interiors, Physical Principles, Structure, and Evolution*. Springer, 2004.

[14] M. Wurm *et al.*, "The next-generation liquid-scintillator neutrino observatory lena", 2012. [Online]. Available: http://wwwth.mpp.mpg.de/members/raffelt/mypapers/201104.pdf.

[15] J. Migenda, *Supernova burst observations with dune*, Presentation at NuPhys2017, Online; accessed 3 June 2018, 2017. [Online]. Available: https://arxiv.org/pdf/1804.01877.pdf.

[16] R. N. Boyd, *An Introduction to Nuclear Astrophysics*. Springer, 2007.

[17] B. Baller *et al.*, ""liquid argon time projection chamber research and development in the United States"", *arXiv*, Sep. 2014. [Online]. Available: https://arxiv.org/pdf/1307.8166.pdf.

[18] Benjamin J. P. Jones, "Sterile Neutrinos in Cold Climates", 2015.

[19] DUNE Collaboration, "The Single-Phase ProtoDUNE Technical Design Report", Tech. Rep., Jul. 2017.

[20] Erica Snider, *Introduction to LArSoft*, Presentation at art/LArSoft Course at Fermilab, August 2015, Online; accessed 15 February 2018, 2015. [Online]. Available: https://indico.fnal.gov/event/9928/session/8/material/2/0.

[21] Alex Himmel, *The DUNE Far Detector and protoDUNEs*, Presentation at 38th International Conference on High Energy Physics in Chicago, Online; accessed 14 February 2018, 2016. [Online]. Available: https://indico.cern.ch/event/432527/contributions/1071670/attachments/1320701/1980467/2016-08-05-ICHEP-himmel-dune-and-protodune.pdf.

[22] R. Acciarri *et al.*, "The Long-Baseline Neutrino Facility (LBNF) and Deep Underground Neutrino Experiment (DUNE) Conceptual Design Report Volume 2", Tech. Rep., Jul. 2015.

[23] R. Acciarri *et al.*, "The Long-Baseline Neutrino Facility (LBNF) and Deep Underground Neutrino Experiment (DUNE) Conceptual Design Report Volume 1", Tech. Rep., Jul. 2015.

[24] K. Hitachi and T. Takah, "Effect of ionizationdensity on the time dependence of luminescence from liquid argon and xenon", *Physical Review B*, vol. 27, no. 9, 1983. [Online]. Available: https://journals.aps.org/prb/pdf/10.1103/PhysRevB.27.5279.

[25] Flavio Cavanna, Ana Machado, Denver Whittington, *Update from the Photon Collection WG*, Presentation at January-February 2018 DUNE Collaboration Meeting at CERN, Online; accessed 14 February 2018, 2018. [Online]. Available: https://indico.fnal.gov/event/14581/session/7/contribution/63/material/slides/0.pdf.

[26] Bruce Howard, Stuart Mufson, Denver Whittington, Chris Macias, *Photon detection design utilizing wavelength-shifting plates and commercial light guides*, Online; accessed 15 February 2018, 2017. [Online]. Available: https://docs.dunescience.org/cgi-bin/private/RetrieveFile?docid=5924&filename=Howard-PhotonCollectorWG-24October2017.pdf&version=2.

[27] E. Segreto, A.A. Machado, C.O. Escobar, E. Kemp, G.A. Valdivies, *ARAPUCA Arrays in protoDUNE*, Presentation at DUNE Photon Detector Review in Chicago, Online; accessed 15 February 2018, 2016. [Online]. Available: https://indico.fnal.gov/event/12081/contribution/18/material/slides/0.pdf.

[28] Pai do Gugu Gaiteiro, *Como construir uma Arapuca*, YouTube video uploaded 24 June 2014, Online; accessed 15 February 2018, 2017. [Online]. Available: https://www.youtube.com/watch?v=ho0CRTP9-k0.

[29] *An introduction to the silicon photomultiplier*, Rev. 6.0, SensL, Feb. 2017.

[30] Vishnu Zutshi and Robert Wilson, *DUNE-SP PDS Photosensor WG*, Presentation at 2018 DUNE Collaboration Meeting at CERN, Online; accessed 4 June 2018, 2017.

[31] K. Yamamoto, R. Yamada , K. Kobayashi , K. Sato , A. Ghassemi, *New improvements to a specialized Multi-Pixel Photon Counter (MPPC) for neutrinoless double-beta decay and dark matter search experiments*, Poster Presentation at 2016 ICHEP, Online; accessed 4 June 2018, 2017. [Online]. Available: https://www.hamamatsu.com/sp/ssd/microsite/MPPC/ICHEP_MPPC_panel_160731.pdf.

[32] *Mppc and mppc module for precision measurement*, Hammamatsu, Mar. 2016. [Online]. Available: https://www.hamamatsu.com/resources/pdf/ssd/mppc_kapd0004e.pdf.

[33] M. Ramilli, "Characterization of sipm", *sensl*, 2017. [Online]. Available: http://www.sensl.com/downloads/irp/2008_Ramilli_Characterization_SiPM_temperature_dependencies.pdf.

[34] *C-series low noise, blue-sensitive silicon photomultipliers datasheet*, SensL, Sep. 2014.

[35] Steven Gardiner, *Simulations of Charged-Current Supernova Events in a Liquid Argon Time Projectoin Chamber*, Presentation at 2016 APS April Meeting, Online; accessed 16 February 2018, 2016. [Online]. Available: https://absuploads.aps.org/presentation.cfm?pid=12396.

[36] S. Gardiner, *MARLEY Tutorial Webinar*, Presented at a SNB/LE Physics Working Group Meeting, Online; accessed 26 June 2018, 2016. [Online]. Available: https://indico.fnal.gov/event/12547/contribution/7/0/material/slides/0.pdf.

[37] R. M. Bionta *et al.*, "Observation of a neutrino burst in coincidence with supernova 1987a in the large magellanic cloud", *Physical Review Letters*, vol. 58, no. 14, Apr. 1987. [Online]. Available: https://journals.aps.org/prl/pdf/10.1103/PhysRevLett.58.1494.

[38] K. H. et al., "Observation of a neutrino burst from the supernova siv1987a", *Physical Review Letters*, vol. 58, no. 14, Apr. 1987. [Online]. Available: https://journals.aps.org/prl/pdf/10.1103/PhysRevLett.58.1490.